Shepherd, K., Namur, O., Neave, D., Zhang, Y., Van Gerve, T., Van Helden, T., Van Acker, T., Klemme, S., Berndt-Gerdes, J., Charlier, B. and Vander Auwera, J. (2026) “Insights into the magma plumbing system architecture beneath an off-ridge ocean island (Terceira, Azores) from crystal zoning”, *Volcanica*, 9(1). doi: 10.30909/vol/vol/cdwz4711.

RESEARCH ARTICLE

VOLCANICA

Insights into the magma plumbing system architecture beneath an off-ridge ocean island (Terceira, Azores) from crystal zoning

Kat Shepherd [α], Olivier Namur *[α], David A. Neave[β], Yishen Zhang[γ], Thomas van Gerve[α], Tom Van Helden[δ], Thibaut Van Acker[δ], Stephan Klemme[ε], Jasper Berndt-Gerdes[ε], Jacqueline Vander Auwera[ζ], and Bernard Charlier[ζ]

[α] Department of Earth and Environmental Sciences, KU Leuven, Leuven 3001, Belgium.
[β] Department of Earth and Environmental Sciences, The University of Manchester, Manchester, M13 9PL, United Kingdom.
[γ] Department of Earth, Environmental and Planetary Sciences, Rice University, 6100 Main Street, MS 126, Houston, TX 77005, USA.
[δ] Atomic and Mass Spectrometry (A&MS) research unit, Department of Chemistry, Ghent University, Campus Sterre, De Pintelaan 270 - S12, 9000, Ghent, Belgium.
[ε] Institut für Mineralogie, Westfälische Wilhelms-Universität Münster, Corrensstraße 24, 48149 Münster, Germany.
[ζ] Department of Geology, University of Liege, 4000 Sart Tilman, Belgium.

Submitted: 2025-08-04 | Accepted: 2026-04-14 | Published: 2026-05-15

Editor: D. Geist | Typesetter: J. Farquharson

Abstract

Understanding the architecture and dynamics of crustal magmatic plumbing systems is essential for interpreting volcanic processes and eruption styles in ocean island settings. We present a comprehensive investigation of the magmatic plumbing system beneath Terceira Island (Azores), integrating petrographic observations, whole-rock geochemistry, high-resolution elemental mapping of clinopyroxene, thermobarometry, and diffusion chronometry to elucidate magma storage and evolution processes. Our results reveal a vertically extensive, multi-level magmatic system comprising interconnected melt pockets and mush zones spanning from the Moho (~400–500 MPa), ~18–20 km depth) to shallow upper crustal levels (~100 MPa), ~3 km depth). High-resolution mapping of major and trace elements in clinopyroxene uncovers zoning (notably in Cr and Ni) providing new constraints on magma recharge and mixing processes. Primitive, Mg-, Cr-, and Ni-enriched basalts ascend from the mantle and pond at deep crustal levels, where interaction with a partially crystallized mush promotes the growth of olivine crystals and complex clinopyroxene zoning. Multiple mafic recharge events at mid-crustal depths (~200–300 MPa) induce dynamic disequilibrium textures and oscillatory zoning in clinopyroxene and plagioclase, reflecting variable pressure-temperature-composition conditions. Shallower reservoirs crystallize evolved, Cr-depleted melts that feed trachytic and rhyolitic eruptions. Timescale modelling suggests pre-eruptive storage durations averaging ~10 months, with maxima reaching up to 8 years. These findings highlight the critical role of crustal architecture and tectonic setting in controlling magma differentiation pathways and eruption styles within ocean islands.

Keywords: Ocean island; Plumbing system; Pyroxene; Plagioclase; Crystal mush; Basalt.

1 Introduction

Oceanic crust forms at mid-ocean ridges, producing mid-ocean ridge basalts (MORBs) through the melting of passively upwelling asthenosphere, and is assumed to reflect the composition of the upper convecting mantle [McKenzie and Bickle 1988; Fitton 2007]. Ocean island volcanism, however, represents enhanced magmatic activity in oceanic intraplate settings associated with hotspots, e.g. Hawai'i [Wilson 1963; Ribe and Christensen 1999], Canary Islands [Carracedo et al. 1998], and the Azores [Schilling 1975; Arnould et al. 2019]. Ocean island basalts (OIBs) are a group of geochemically distinctive rocks that are typically associated with ocean islands and seamounts. OIBs are produced by decompression melting of mantle that, due to thermal buoyancy, is actively upwelling in mantle plumes [Maclennan et al. 2001; O'Neill 2016]. Plumes have a high mantle potential temperature (i.e. temperature that a parcel of mantle rock would have if it were adiabatically decompressed to the surface without undergoing melting) so the start of melting is deeper than for passive upwelling in mid-ocean ridges. However, mantle upwelling is typically impeded by the thicker lithosphere present in intraplate settings, so melting stops at greater depths than beneath mid-ocean ridges. This lithospheric-lid effect greatly influences the major and trace element geochemistry of OIBs [e.g. Humphreys and Niu 2009; Niu et al. 2011], which are geochemically and isotopically distinct from MORB and often alkalic in nature [Davies et al. 1995]. For example, OIBs are generally more enriched in incompatible trace elements (e.g. rare earth elements) than MORBs, due to either more enriched sources than MORBs or lower degrees of partial melting [McKenzie and O'Nions 1995; Hofmann 2003; Dasgupta et al. 2010]. However, the ways in which the enriched compositions of OIBs reflect their storage and evolution during ascent remain uncertain, though the relatively low magma flux experienced by many ocean island volcanoes may produce transient and compartmentalised magma reservoirs that are reflected in the textural and geochemical complexity of erupted magmas and crystal cargoes [Chamberlain et al. 2019; Kahl et al. 2021; Scarrow et al. 2024]. Moreover, magmatic processes may operate at greater depths beneath ocean islands than beneath mid-ocean ridges [Klügel et al. 2015; Li et al. 2025], affecting the compositions of erupted lavas in important but underexplored ways [Ubide et al. 2021].

* olivier.namur@kuleuven.be

The Azores archipelago is located in the North Atlantic Ocean. It is a group of OIB-producing volcanic islands that straddle the Mid-Atlantic Ridge (MAR) to the east and west. Magmatism in the Azores is widely understood to originate from the interaction between the MAR and a deep mantle plume [Schilling 1975; Moreira et al. 1999; Madureira et al. 2005; Beier et al. 2010; Madureira et al. 2014], though the nature of the plume remains contested. Terceira is the third largest island in the archipelago and volcanism on the island ranges from alkali basalt lava flows to trachytic lavas and pyroclastic material [Self 1976; Mungall and Martin 1995]. The last subaerial eruption was in 1761 [Pimentel et al. 2016], which produced extensive lava flows and contemporaneous trachyte effusion. It was followed by two submarine eruptions in 1867 and 1998–2001 [Casas et al. 2018]. Although the most recent eruptions on Terceira have been basaltic, ignimbrite-forming eruptions are well documented [e.g. Gertisser et al. 2010; Jeffery et al. 2017; Pimentel et al. 2021]. This is because they pose a greater risk to the population due to their high explosivity, though basaltic eruptions are not without hazard [e.g. Del Fresno et al. 2023]. Terceira thus offers excellent opportunities for investigating how magma storage conditions and magma reservoir processes such as crystal fractionation affect the geochemistry of erupted OIB magmas within the Azores and beyond [e.g. Zanon et al. 2024].

The texture and composition of minerals such as olivine, clinopyroxene, and plagioclase in magmatic rocks can offer insights into magma chamber processes. Crystal zoning develops in response to variations in growth conditions, forming mineral–melt boundary layers, or to changes in melt composition, pressure or temperature [e.g. Mollo and Hammer 2017; Caracciolo et al. 2021; Andrews 2022]. Zoning is preserved when the diffusion rate is low enough that chemical relaxation does not not fully take place during magma storage [Costa et al. 2008; Kahl et al. 2011; Dohmen et al. 2017; Costa et al. 2020], and can occur in key rock-forming minerals such as olivine [Costa et al. 2010; Kahl et al. 2011; 2017; Couperthwaite et al. 2022], clinopyroxene [Ubide et al. 2015; Welsch et al. 2016; Ubide et al. 2019a; b; Schoneveld et al. 2020; Palummo et al. 2021; Tapu et al. 2022; Neave et al. 2024], and plagioclase [Hattori and Sato 1996; Tepley and Davidson 2003; Churikova et al. 2013; Namur et al. 2014; Namur and Humphreys 2018; Van Gerve et al. 2020].

Clinopyroxene is particularly useful for reconstructing the history of magma plumbing systems and timescales of magmatic processes as it is stable throughout the upper mantle and crust and is characterised by relatively low chemical diffusivities for REE (e.g. $\log D = 1 \times 10^{-18}$–$1 \times 10^{-21}$ $m^2 s^{-1}$ at 1200 °C; D = diffusion coefficient), Fe–Mg and Cr [Van Orman et al. 2001; Müller et al. 2013]. This means that primary features are retained during subsequent storage and processing. The composition of clinopyroxene is also sensitive to changes in the pressure, temperature, composition and volatile content [Putirka 2008; Neave and Putirka 2017; Mollo et al. 2018] of its carrier melts, and the distribution and concentration of elements in its crystal structure is recorded in a diverse range of textures that may offer insights into the nature of the oceanic crust.

Here we apply a combination of detailed petrography, bulk chemical analysis and in situ major and trace element analysis on a suite of samples from Terceira to identify pre-eruptive processes and determine magma storage conditions within the sub-volcanic plumbing system. We apply a detailed multi-method mapping approach, combining electron probe microanalysis (EPMA) and laser ablation-inductively coupled plasma-time of flight-mass spectrometry (LA-ICP-TOF-MS) maps for a detailed investigation of major and trace element zoning patterns. Petrological results, textural observations and pressure-temperature (P–T) estimates of clinopyroxene crystallisation offer new insights into deep magma dynamics and the architecture of the oceanic crust beneath Terceira.

2 Geological setting

The Azores archipelago is a geodynamically complex region situated at the triple junction between the Nubian, Eurasian, and North American plates (Figure 1A), and bound by three major tectonic features: (1) the MAR, which delimits the North American and Eurasian plates; (2) the East Azores Fracture Zone (EAFZ), a seismically-inactive transform fault system on the southern margin of the plateau thought to be a relic boundary between the Nubian and Eurasian plates [Searle 1980]; (3) the Terceira Rift [Machado 1959], a hyperslow spreading centre [Vogt and Jung 2004] with a spreading rate of 2 to 4 mm yr^{-1} that marks the currently active boundary between the Eurasian and Nubian plates. The Terceira Rift is defined by a series of basins, seamounts, and the volcanic islands of Graciosa, Terceira, and São Miguel.

Thick oceanic crust, such as that beneath the Azores (17–29 km; [Zanon et al. 2023]) requires either higher degrees of melting than normal or active upwelling [Asimow et al. 2004; Madureira et al. 2005]. It is widely believed that the Azores plateau originates from the interaction between the MAR and a melting anomaly. The upwelling of an unusually hot or volatile-enriched mantle [Schilling 1975; White et al. 1979; Schilling 1985; Bonatti 1990; Asimow et al. 2004; Beier et al. 2012; Métrich et al. 2014; van Gerve et al. 2024; Li et al. 2025] is believed to have resulted in extensive melting and the formation of volcanic activity in the eastern part of the plateau. Indeed, Cannat et al. [1999] suggested that an episode of enhanced magmatism some 10 Ma ago, reflecting excess temperatures of ca. 70 °C in the mantle beneath the ridge, drove this increased melting and played a significant role in the construction of the Azores plateau. Several geophysical [Adam et al. 2013] and geochemical [Madureira et al. 2014] studies have attributed this melting anomaly to a mantle plume-like feature, the location of which is thought to lie beneath Terceira [Bourdon et al. 2005; Madureira et al. 2005] or one of the other central islands, e.g. Faial [Shorttle et al. 2010] or São Jorge [Beier et al. 2012].

The island of Terceira is formed from four large volcanoes: Cinco Picos in the east, Guilherme Moniz and Pico Alto in the centre, and Santa Barbara in the west. It is also bisected by a NW–SE trending basaltic fissure zone, the subaerial expression of the Terceira Rift [Nunes et al. 2014; Jeffery et al. 2017]. Products from volcanic centres show compositions that range from basaltic to trachytic (47–68 wt.% SiO_2; Mungall

and Martin [1995], Gertisser et al. [2010], and Jeffery et al. [2017]), though fissure basalts show a narrower compositional range (46–50 wt.% SiO_2; Zanon and Pimentel [2015]). The eastern third of the island is dominated by the heavily eroded 7 km-wide caldera of Cinco Picos volcano (Figure 1b), the oldest edifice on the island dated at 401 ± 6 ka [Hildenbrand et al. 2014]. This caldera is partially filled and buried by the products of more recent volcanoes and fissure basalts. The products of this extinct volcano comprise hawaiitic to mugearitic lavas, trachytic lavas and pyroclastic deposits [Self 1976; Self and Gunn 1976; Madeira 2005; Gertisser et al. 2010]. In the centre of the island is the elongate caldera of Guilherme Moniz (Figure 1b), an extinct volcano active prior to 270 ka that produced hawaiitic lavas to comenditic coulées and ignimbrites [Self 1976; Self and Gunn 1976; Gertisser et al. 2010]. The caldera floor is partially filled by fissure basalts, and the northern sector of the caldera is almost completely covered by more recent lava domes and coulées from Pico Alto [Self and Gunn 1976; Madeira 2005; Gertisser et al. 2010]. North of Guilherme Moniz is the smaller caldera of Pico Alto volcano (Figure 1b), which is entirely filled by a cluster of pantelleritic coulées and lava domes [Gertisser et al. 2010]. Activity on Pico Alto began over 141 ka and was dominated by violent eruptions, producing trachytic ignimbrites, lava flows and pumice fall and surge deposits [Self 1976; Self and Gunn 1976; Mungall and Martin 1995; Calvert et al. 2006; Gertisser et al. 2010; Pimentel et al. 2021]. The last ignimbrite-forming period on Pico Alto was between 20–23 ka during which the Lajes-Angra Ignimbrite Formation (LAI) was produced, an extensive formation which comprises the Angra Ignimbrite, exposed only on the southern coast, and the Lajes Ignimbrite which is exposed on both the north and south coasts [Gertisser et al. 2010]. The western third of the island is occupied by Santa Bárbara volcano, a young (65 ± 13 ka; Hildenbrand et al. [2014]) stratovolcano with two small overlapping calderas at the summit (Figure 1b). The inner caldera is in-filled by trachytic lava domes, and several alignments of domes and coulées line the flanks of the volcano [Self 1976; Self and Gunn 1976; Calvert et al. 2006; Pimentel et al. 2021]. Products of the volcano include hawaiite and mugearite lavas overlain by recent (20–23 ka) peralkaline silicic lava domes, coulées and pumice falls [Self 1976; Self and Gunn 1976; Jeffery et al. 2017]. The most recent activity associated with Santa Bárbara was the formation of eight trachytic domes and coulées in A.D. 1761 on the eastern flank of the volcano [Calvert et al. 2006; Nunes et al. 2014].

The Basaltic Fissure Zone (BFZ) is a 2 km-wide alignment of basaltic to hawaiitic scoria cones, spatter cones and lava flows that bisects the island in a WNW–ESE direction and becomes progressively younger towards the NW. It traverses the extinct Cinco Picos and Guilherme Moniz volcanoes in the SE and continues offshore along the Serrata Ridge in the NW for several kilometres [Zanon and Pimentel 2015; Madureira et al. 2017]. The BFZ dates to at least 43 ka [Calvert et al. 2006], but is likely contemporaneous with the island itself. Recent activity along the BFZ comprises a paired subaerial eruption in the centre of the island (Figure 1b) in 1761 [Pimentel et al. 2016], and two submarine eruptions along the Serreta Ridge in 1867 and 1998–2001 [Gaspar et al. 2003; Casas et al. 2018].

The volcanic products of Terceira are divided stratigraphically into two groups: (1) the Upper Terceira Group, marked by the base of the LAI [Self 1976], which comprises the products of at least 116 eruptions from the BFZ and the active Santa Bárbara and Pico Alto volcanoes, and (2) the Lower Terceira Group, which encompasses the interstratified pyroclastic fall deposits, ignimbrites and lava flows predating the LAI [Gertisser et al. 2010]. A detailed description of the relative volumes of volcanic rocks erupted before and after LAI for each volcanic complex of Terceira is reported in Pimentel [2015]. Here we sample products predominantly from the Upper Terceira Group, which are identifiable by their stratigraphic position above the LAI, with a focus on obtaining a range of (dominantly basaltic) compositions to better constrain the plumbing system beneath Terceira.

3 Samples and methods

Sixty-one samples were collected from the coastline and along the basaltic fissure zone axis in the centre and south east of the island during fieldwork in September 2020 (Figure 1b). A range of samples from juvenile basalts to more evolved felsic deposits were collected from the fissure zone and around volcanic centres. However, the suite of evolved samples collected is incomplete as we focussed on collecting the (seemingly) most primitive rocks from each region of the island; nonetheless, a small selection of felsic samples were collected, where well-exposed. Samples containing mud-filled vesicles were discarded. Sample names are presented in Electronic Appendix (EA).

3.1 Petrographic observations

Sample petrography was observed using a Nikon optical microscope under transmitted and reflected light, and backscattered electron (BSE) images were obtained with a TESCAN MIRA 4 scanning electron microscope (SEM) at KU Leuven (Belgium) using a fixed working distance of 13 mm, an accelerating voltage of 15 kV and beam current of 100–300 nA. Following the classification of Zellmer [2021], we refer to crystals with a long axis of ≥ 10 mm as megacrysts, ≥ 500 µm to < 10 mm as macrocrysts and those <500 µm in length and ≤ 30 µm in width as microcrysts. We favour these terms over the terms phenocryst and microphenocryst as they eliminate any genetic connotation with the carrier liquid. Vesicularity and crystal phase proportions were determined by point counting of at least 1000 randomly sampled points on polished thin sections using the freeware JMicroVision v1.3.4. The following phases were counted: megacrysts and macrocrysts of olivine, clinopyroxene, plagioclase, oxides, plus vesicles and groundmass; groundmass crystal phases were not counted towards single crystal total proportions, but rather towards the total groundmass fraction. For crystals exhibiting optical and/or compositional zoning, the inner zone of relatively constant composition is defined as the *core*, whereas the outer zone of constant or progressively varying composition is referred to as the *rim*. When an intermediate textural or compositional zone occurs between the core and rim, it is described as the *mantle* [Namur et al. 2014].

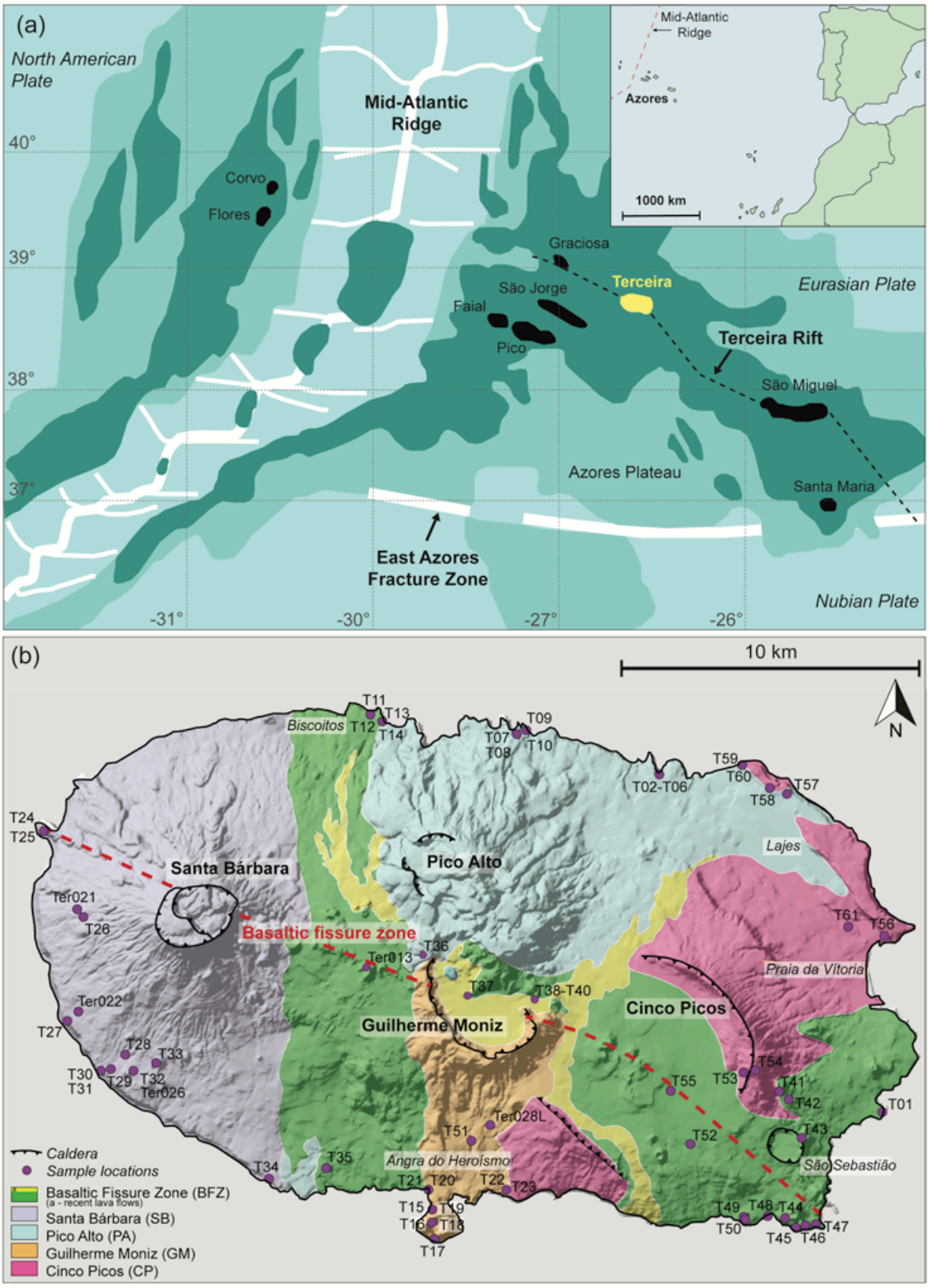

Figure 1: (a) Location of the Azores archipelago relative to major tectonic features and plate boundaries of the Azores plateau and (inset) location of the archipelago relative to continental Europe and Africa. Modified after [Luis1994; Lourenco1998; Searle 1980]. Green-scale corresponds to bathymetric depth. (b) Simplified geological map of Terceira highlighting volcanic centres (in bold), major settlements (in italics), and sample locations (purple circles). Modified after [Madeira 2005; Gertisser et al. 2010; Nunes et al. 2014].

Crystallographic orientations of olivine crystals were determined by electron backscatter diffraction (EBSD) at Heidelberg University using a JEOL IT800 field emission gun scanning electron microscope (FEG-SEM), equipped with an Oxford Instruments Symmetry2 EBSD detector. The FEG-SEM was operated with an accelerating voltage of 18 kV, a 9.4 nA beam current, and the sample was tilted by 70°. Orientation maps comprising hundreds of EBSD points were obtained for each crystal and subsequently averaged in order to minimise analytical uncertainty and provide an overview of different orientations within the same crystal. This comprehensive approach is superior to random measurements of a few selected points across the crystal and enables the identification of features such as internal lattice misorientations, sub-grain boundaries, crystal twins, and pseudo-symmetries. The EBSD maps were obtained at a working distance of 27–28 mm using a 10 µm step size and a Hough transform resolution of 75. Measured Euler angles were converted into trends and plunges of the olivine crystallographic *a*-, *b*-, and *c*-axes. The angles between the measured electron microprobe traverses and the crystallographic *a*-, *b*-, and *c*-axes in olivine were calculated using the Stereo32 software developed at the Ruhr-Universität Bochum [Kahl et al. 2015].

3.2 Whole rock chemistry

All samples were crushed with a hammer and ground into fine powders with agate mortars in a Fritsch Pulverisette 7 planetary mill. Loss on ignition (LOI) was determined by dehydrating and oxidizing 1 g of each sample at 1000 °C for 2 hours in a ceramic crucible in a muffle furnace. Whole-rock major and select trace element (Co, Cu, Ni, Rb, Sr, Y, Zn, Zr, Ba, Cr and V) concentrations were measured by X-ray fluorescence (XRF) with an ARL PERFORM-X 4200 (Rh X-ray tube) at the University of Liège (Belgium) using a method similar to that described by Vander Auwera et al. [2019]. Results are reported in EA (Appendix). Major element analyses were performed on lithium tetra- and meta-borate fused glass discs prepared with 0.35 g of rock powder and raw data were corrected following the Traill–Lachance algorithm, calibrated with 66 international rock, mineral and soil standards. Trace element analyses were performed on pressed powder pellets and raw data (except Cr and V) were corrected for matrix effects by Compton peak monitoring. Major element accuracy is estimated to be better than ±2 % relative for all element oxides except Na_2O (±8.1 %) and MnO (±4.4 %). Analytical precision (1σ standard deviation; SD) was estimated by repeated analyses of nine in-house standards (42 measurements of each standard) and estimated to be better than ±5 % for all major element oxides except Na_2O (±6.6 %). Accuracy of minor and trace element measurements was estimated from repeat analyses of BHVO-1, STM-1, and SY-2 and was better than ±10 % for all trace elements except Cu (±26 %). Analytical precision (1σ) was estimated to be better than ±3 % for all trace elements except Co (±6 %). Additional details on precision, accuracy and limits of detection can be found in Namur et al. [2020].

For further trace element characterisation, all samples were analysed by inductively coupled plasma-mass spectrometry (ICP-MS) at KU Leuven (Belgium) using an Agilent 7700x (Agilent Technologies, Tokyo, Japan). The following elements were determined: ^{9}Be, ^{51}V, ^{58}Ni, ^{59}Co, ^{63}Cu, ^{64}Zn, ^{69}Ga, ^{85}Rb, ^{88}Sr, ^{89}Y, ^{90}Zr, ^{93}Nb, ^{98}Mo, ^{133}Cs, ^{138}Ba, ^{139}La, ^{140}Ce, ^{141}Pr, ^{142}Nd, ^{152}Sm, ^{153}Eu, ^{158}Gd, ^{159}Tb, ^{164}Dy, ^{165}Ho, ^{166}Er, ^{169}Tm, ^{174}Yb, ^{175}Lu, ^{180}Hf, ^{181}Ta, ^{208}Pb, ^{232}Th, and ^{238}U, and are reported in EA (Appendix). Samples were prepared according to the following method: for each sample, 100 mg of finely crushed powder was added to 500 mg of $LiBO_2$ and fused in a graphite crucible at 1000 °C for 10 minutes. The molten material was then dropped into 50 g of 3% HNO_3 and mixed continuously on a stage with a magnetic stirrer for 10 minutes until homogeneous. The preparation was then left to cool overnight, and 0.4 mL of the solution was diluted with 9.6 mL of 5% HNO_3 and spiked with 1% Ge, In, and Ir in a 5 mg/L mixed solution to be used as an internal standard. The international basaltic standards BCR-1 and BR, as well as the granite standard GA, were prepared in the same manner and analysed alongside the unknowns, in addition to five replicate samples and two blanks. Accuracy of trace element measurements was estimated by repetitive analyses of several international (from the GeoREM database; Jochum et al. [2005]) and in-house standards, and was better than ±10 % for all trace elements. Analytical precision (1σ) was estimated as better than 10% for most elements. All whole rock data are reported in Electronic Appendix EA1.

3.3 In situ mineral analyses

Quantitative in situ measurements of mineral phases (olivine, plagioclase, clinopyroxene and Fe-Ti oxides) were obtained by EPMA using JEOL JXA-8530F and JEOL JXA-8900 electron microprobes hosted at the Department of Material Engineering, KU Leuven (Belgium) and the Institut für Mineralogie, University of Münster (Germany), respectively, and are reported in EA (Appendix).

The electron beam parameters were set to 15 kV accelerating voltage and 20 nA beam current, with counting times of 10 s (peak) and 5 s (background) for all elements. Na was measured first to minimise loss. The measured X-ray intensities were corrected using the ZAF procedure (Z: atomic number; A: absorption; F: fluorescence). The Kα calibration standards used were forsterite (Mg), fayalite (Fe), wollastonite (Si, Ca), albite (Na), orthoclase (K), chromite (Cr), olivine (Ni), $MnTiO_3$ (Mn, Ti), and Al_2O_3 (Al).

To ensure internal consistency across multiple analytical sessions, EPMA results were normalised to international standards: Kakanui augite (NMNH 122142) was used as an internal standard for clinopyroxene and plagioclase analyses, and San Carlos olivine (NMNH 111312–44) for olivine analyses. Spot analyses were conducted along transects across the crystals with a constant spacing, typically 5 µm, or as individual points in sector-zoned crystals. Accuracy and precision were estimated by repeated analyses of in-house and Smithsonian microbeam standards of augite [Jarosewich et al. 1980], plagioclase [An_{95}; An = 100 Ca/(Ca + Na), mol %] and olivine (Fo_{83} and Fo_{10}; Fo = 100 Mg/(Mg + Fe), mol %). Repeat analyses yielded reproducibility better than ±5 % for major elements and accuracy within ±5 % for most elements.

Magnetite and ilmenite major- and minor-element compositions (EA; Appendix) were measured by EDX with an Oxford Xplore30 detector coupled with a Tescan Mira 4 SEM at KU Leuven (Belgium). Analyses were performed with a 15 kV accelerating voltage and a 6 nA beam current, and calibration was done using the extended factory calibration included in the Oxford Aztec software. The measurements are unnormalized, using analyses of pure Mn for beam calibration. Repeat measurements of reference materials (magnetite: NMNH114887, ilmenite: NMNH96189; Jarosewich [2002]) indicate major-element accuracies and precisions of approximately 3 %.

Trace element concentrations in selected clinopyroxenes, reported in EA (Appendix), were measured in situ by laser ablation coupled to tandem ICP-mass spectrometry (LA-ICP-MS/MS). An Analyte G2 ArF* excimer-based 193 nm laser ablation system (Teledyne Photon Machines, Bozeman, USA) was coupled to an Agilent 8900 tandem ICP-mass spectrometer (Agilent Technologies, Tokyo, Japan) via the aerosol rapid introduction system (ARIS Van Malderen et al. [2015]) at KU Leuven (Belgium). Helium was used as the aerosol carrier gas and Ar make-up gas was added downstream via a coaxial mixing bulb, along with 5 mL/min of N_2 gas to boost the sensitivity. The instrument was tuned for high sensitivity across the elemental mass range using NIST SRM 612 glass [Jochum et al. 2011], while minimizing elemental fractionation ($^{238}U^+/^{232}Th^+ = 1$) and oxide ion formation ($^{238}U^{16}O^+/^{238}U^+ < 0.5\%$). The following nuclides were measured at a dwell time of 10 ms: ^{28}Si, ^{45}Sc, ^{48}Ti, ^{51}V, ^{52}Cr, ^{55}Mn, ^{59}Co, ^{58}Ni, ^{63}Cu, ^{64}Zn, ^{88}Sr, ^{89}Y, ^{90}Zr, ^{93}Nb, ^{138}Ba, ^{139}La, ^{140}Ce, ^{141}Pr, ^{142}Nd, ^{152}Sm, ^{153}Eu, ^{158}Gd, ^{159}Tb, ^{164}Dy, ^{165}Ho, ^{166}Er, ^{169}Tm, ^{174}Yb, ^{175}Lu, ^{180}Hf, ^{181}Ta. The samples were pre-ablated at low fluence using a raster pattern to remove any surface contamination. Each analytical batch was comprised of up to 20 analyses, and spot analysis was performed using a laser repetition rate of 10 Hz and a fluence of 3.5 J cm^{-2}, with spot sizes between 35–50 µm, depending on the crystal size. Each 30 s ablation was preceded by 20 s blank and followed by 30 s washout. NIST SRM 612 glass was measured twice at the beginning and twice at the end of each batch for external calibration. Ca concentrations from EPMA (21.5 ± 0.7 wt % CaO; n = 1285) were used as an internal standard for clinopyroxene to correct for differences in ablation yield, matrix effects and instrumental signal drift. Accuracy and precision were monitored using the MPI-DING glasses GOR-128, GOR-132 and ML3B [Jochum et al. 2006]. Most trace elements were determined with an accuracy better than ±10 % compared to published values. Elements with recoveries outside this range were excluded. Repeat analyses yielded 1σ relative precision of ±5–10 % for all measured elements.

3.4 Semi-quantitative EPMA maps

Semi-quantitative major element maps (SF1; Appendix) were obtained for a total of 32 clinopyroxene crystals from nine samples using a JEOL JXA-8900 EPMA at the University of Münster (Germany). A beam current of 60–80 nA and an accelerating voltage of 15 kV were used, with a pixel size of 2–5 µm and a dwell time of 20 ms per pixel. Ten elements (Si, Ti, Al, Fe, Mn, Mg, Ca, Na, K, Cr) were measured per analysis (two per diffracting crystal). Mapped areas varied in size from 300 × 300 µm^2 to 5000 × 5000 µm^2. Total experiment times ranged from 0.5 to 12 hours per crystal.

3.5 Quantitative Multi-Element LA-ICP-TOF-MS maps

To gain further insight into the nature of chemical zoning in clinopyroxene quantitative LA-ICP-TOF-MS maps of 11 crystals were obtained at University of Ghent (Belgium) and combined with transmitted light and/or BSE images (SF2; Appendix). LA-ICP-TOF-MS is capable of monitoring essentially the entire elemental mass range at high spatial resolution (< 10 µm) and provides low detection limits [Ubide et al. 2019a], and as such can be used to delve further into the behaviour of trace elements recorded in zoned crystals. A setup consisting of an Iridia LA unit (Teledyne Photon Machines, Bozeman, USA) equipped with a 193 nm ArF* excimer-based laser, Cobalt ablation chamber and cup-type ablation cell was coupled via the ARIS to an icpTOF 2R (TOFWERK AG, Thun, Switzerland). Helium was used as carrier gas (0.5 L/min) and Ar make-up gas (0.92 L/min) was added via the ARIS mixing bulb prior to introduction of the aerosol into the plasma. A laser spot size of 5 µm (square mask), repetition rate of 50 Hz and a fluence of 6.5 J/cm^2 were used for elemental mapping that involved firing a single shot per pixel position at a lateral scan speed of 250 µm/s. The Iridia laser ablation system was operated with Chromium v2.7. software (Teledyne CETAC), and the icpTOF 2R was operated with TOFPilot software (TOFWERK AG). The instrumental setup was tuned upon ablation of a NIST SRM 610 glass for high sensitivity across the elemental mass range (based on $^{59}Co^+$, $^{115}In^+$, $^{238}U^+$), low oxide ion formation ($UO^+/U^+ < 0.5\%$) and low elemental fractionation ($^{238}U^+/^{232}Th^+ = 1$). NIST SRM 610 and 612 glasses were used as external calibration standards, and Ca obtained by EPMA was used as the internal standard (21.5 ± 0.7 wt.% CaO; n = 1,285). Accuracy and precision were evaluated using the MPI-DING glasses GOR-128, GOR-132, and ML3B [Jochum et al. 2006]. Quantitative elemental maps were produced with Iolite v4.5.1 [Paton et al. 2011]. To interrogate the elemental maps in further detail, average elemental compositions were extracted from profiles along the crystal axes and regions of interest (ROI) in homogeneous areas, i.e. free of cracks, holes or strong zonation features, to obtain high-precision concentration data by averaging a large number of data points from within the homogeneous ROIs (SF3 and EA; Appendix).

3.6 Thermobarometry and oxybarometry calculations

Where both ilmenite and Ti-magnetite were present, temperature and fO_2 estimates were calculated using the two-oxide Microsoft Excel spreadsheet of Sauerzapf et al. [2008] – referred to here as model S08. Equilibrium between mineral pairs was evaluated using the Mn–Mg partitioning test of Bacon and Hirschmann [1988].

Estimating crystallisation temperatures and pressures typically requires knowledge of mineral and their equilibrium melt compositions. However, we did not find groundmass glass or fresh, glassy melt inclusions in our samples, so identifying equilibrium liquid compositions is challenging. To

circumvent this issue, we applied thermobarometric formulations that require only mineral compositions. To obtain more robust pressure (P, MPa) and temperature (T, °C) estimates, we used two different clinopyroxene-only models: the machine learning algorithm of Jorgenson et al. [2022], referred to here as model J22 and the iterative algorithm implemented in the Python3 tool `Thermobar` (v1.0.16, Wieser et al. [2022]), which iterates equations 32b and 32d of Putirka [2008], referred to as model P08. We also tested the GAIA deep learning-based tool of Chicchi et al. [2023], referred to here as model C23 but found out that this model gives unrealistically low pressue estimates, as previously reported [Ágreda-López et al. 2024]. Reported uncertainty on model J22 is shown as the interquartile range of the voting distributions, as recommended by Jorgenson et al. [2022] and the standard error of model P08 is reported as ±87 °C and ±260 MPa.

To further assess the reliability of our models, we also applied clinopyroxene–liquid thermobarometry using bulk-rock compositions from Terceira compiled from the GEOROC database and using experimentally produced melts of Neave et al. [2019] as input liquid compositions. We used the clinopyroxene–melt barometer of Neave and Putirka [2017], referred to as NP17. We used a clinopyroxene–melt matching approach in which clinopyroxene compositions are randomly paired with bulk-rock and liquid compositions and iteratively evaluated for equilibrium conditions. Candidate pairs are screened using equilibrium tests based on $Kd^{\mathrm{cpx-melt}}_{\mathrm{Fe-Mg}}$, as well as the diopside–hedenbergite, enstatite–ferrosilite, and Ca–Tschermak components. Accepted pairs satisfy $Kd^{\mathrm{cpx-melt}}_{\mathrm{Fe-Mg}}$ within ±0.03, and other component tests within 2 SEE, following the criteria of Putirka [1999] and Putirka [2008] and Mollo et al. [2013]. This approach follows previously established frameworks [Winpenny and Maclennan 2011; Neave and Putirka 2017; Stock et al. 2018; Gleeson et al. 2020].

3.7 Diffusion modelling in clinopyroxene and olivine

Fe–Mg compositional profiles in both clinopyroxene and olivine were used to model the timescales between magma mixing and eruption at Terceira. For clinopyroxene, timescales were determined using the non-isothermal diffusion incremental step (NIDIS) method of Petrone et al. [2016]. This method uses high-resolution BSE images acquired via SEM, calibrated against the Mg# of clinopyroxene as determined by EPMA. The NIDIS model accounts for the influence of varying temperatures in different magmatic environments – reflected in different Mg# or greyscale values – on diffusion rates to compute the residence time, Δt. The diffusion coefficient is calculated using the Arrhenius equation considering Fe–Mg exchange in clinopyroxene:

$$D = D_0\, e^{-\Delta H/(RT)} \tag{1}$$

where D_0 is the pre-exponential factor [$\log D_0 = -0.02$ m^2 s^{-1}], ΔH is the activation energy [406 kJ mol^{-1}], R is the gas constant [8.3145 J mol^{-1} K^{-1}], and T is the temperature [K].

The NIDIS model calculates Δt using a backward approach from the last-formed compositional boundary, i.e. Δt_2 inwards to the more recent boundary, Δt_1. The calculated total residence time, Δt, corresponds to the time from mafic input to eruption. A more detailed description of the methodology and application to zoned clinopyroxenes is presented in Petrone et al. [2016], Petrone and et al. [2022], and Nardini et al. [2024].

For olivine, Fe–Mg interdiffusion profiles were modeled using one-dimensional finite-element diffusion models based on Fick's Second Law. Elemental concentrations along measured transects were represented using linear finite elements. For a profile of total length L, the spatial domain was discretized using a standard mesh of 300 nodes.

Diffusion was described using a spatially dependent formulation of Fick's Second Law:

$$\frac{\partial C}{\partial t} = \frac{\partial}{\partial x}\left(D(x)\frac{\partial C}{\partial x}\right) \tag{2}$$

where C represents the Fe–Mg concentration and $D(x)$ is the effective diffusion coefficient along the profile [Mutch et al. 2019]:

$$\ln D^{i}_{[001]} = a_i + b_i \ln f_{O_2} + c_i X_{\mathrm{Fo}} + \frac{q_i + h_i P}{T} + j_i P + k_i \ln a_{SiO_2} \tag{3}$$

where $aSiO_2$ was estimated using bulk-rock chemistry at magmatic temperature using MAGEMin [Riel et al. 2022]. To account for the strong crystallographic anisotropy of Fe–Mg diffusion in olivine, the effective diffusion coefficient parallel to the measured profile (D_p) was calculated from the principal diffusion coefficients along the crystallographic axes [Mutch et al. 2019]:

$$D_p = D_{[100]}\cos^2\alpha + D_{[010]}\cos^2\beta + D_{[001]}\cos^2\gamma \tag{4}$$

where α, β, and γ are the angles between the measured profile and the crystallographic axes [100], [010], and [001], respectively. $D_{[100]}$, $D_{[010]}$, and $D_{[001]}$ are the diffusion coefficients parallel to these axes.

Uncertainties in the calculated diffusion timescales were quantified using a Monte Carlo approach. Pressure (P), temperature (T), and oxygen fugacity (fO_2) were treated as variables with associated uncertainties (see details below). For each Monte Carlo realization, values of P, T, and fO_2 were randomly sampled from normal distributions defined by their mean values and standard deviations. These parameters were then used to calculate the diffusion coefficients along the crystallographic axes and the resulting effective diffusivity D_p. For each simulation, the best fit solution was determined by χ^2 minimization between measured and modelled compositional profiles. Reported errors correspond the 5^{th} and 95^{th} percentiles.

4 Results

4.1 Petrography

In general, Terceira lavas are vesicular and may be porphyritic (< 40 vol.% crystals). Our samples can be broadly divided according to sample location and the eruptive centre from which

they originate: Cinco Picos caldera (CPC), eastern fissure zone (EFZ), central fissure zone (CFZ), Monte Brasil (MB), Pico Alto volcano (PAV), and the Santa Bárbara complex (SBC). Petrographic descriptions are based on hand specimens, thin section observation, and point counting results. The mineral assemblage of mafic lavas consists of olivine (5–76 vol.% total micro- and macrocrysts), clinopyroxene (0–69 vol.%), plagioclase (4–79 vol.%), magnetite (0–5 vol.%) and ilmenite (0–7 vol.%) with rare K-feldspar xenocrysts. Felsic lavas consist of alkali feldspar (7–40 vol.%), clinopyroxene (2–7 vol.%) and minor amounts of Fe-Ti oxides and apatite with rare biotite.

4.1.1 *Cinco Picos Caldera (CPC)*

Due to the age and limited accessibility of the Cinco Picos volcano, and the abundance of more recent volcanic material within the caldera, only one sample was collected from the CPC caldera rim. The sample is a highly vesicular basalt (Figure 2A) with sparse, weathered plagioclase microcrysts and highly altered olivine macrocrysts (≤ 1 vol.%) set in a fine-grained, microcrystalline plagioclase-dominated groundmass with magmatic flow structures.

4.1.2 *Eastern Fissure Zone (EFZ)*

Fissure zone samples are divided into two groups: the eastern (EFZ) and central (CFZ) fissure zone. The EFZ comprises mafic pahoehoe and massive lavas (up to 10 m thick) from the floor of the extinct CPC volcano, on- and off-axis lavas, and monogenetic cones in the eastern and southeastern portions of the island. Samples are vesicular (13–42 vol.%) and porphyritic with a mineral assemblage comprising subhedral to euhedral ≤ 3 mm (long axis) clinopyroxene macrocrysts (15–25 vol.%), subhedral plagioclase (2–17 vol.%) and subhedral to euhedral olivine (3–9 vol.%). Samples from a large cone to the south of the CPC caldera are dominated by plagioclase crystals with fewer olivine and clinopyroxene crystals (Figure 2B). Olivine crystals tend to be strongly zoned and sometimes exhibit iddingsite within fractures and/or around the rims, and often contain (crystallized) melt inclusions. Clinopyroxene crystals frequently exhibit oscillatory or sector zoning, and frequently contain melt inclusions. The groundmass (53–87 vol.%) is largely microcrystalline (Figure 2C) anFigure 2D dominated by plagioclase. Opaque Fe-Ti oxides are abundant in the matrix and, rarely, as microcrysts.

4.1.3 *Central Fissure Zone (CFZ)*

On- and off-axis basaltic rift lavas and monogenetic scoria cones from the central part of the island, within the Guilherme Moniz crater and at the northern coast around the town of Biscoitos comprise the CFZ group. Lavas from the CFZ have varying degrees of vesicularity (4–23 vol.%); vesicles tend to be elongated, ranging in size from 0.5 to 9 mm along the long axis. Central CFZ lavas are moderately porphyritic with a mineral assemblage comprising up to 2 mm (long axis) euhedral clinopyroxene (3–6 vol.%), large (~ 2 mm) subhedral to anhedral olivine (1–3 vol.%) and euhedral to subhedral plagioclase (≤ 1 vol.%) with minor Fe-Ti oxides in a microcrystalline plagioclase-dominated groundmass. Melt inclusions were identified in some clinopyroxene and olivine crystals. Sparse xenocrystic subhedral and rounded alkali feldspar crystals with a dark reaction rim are present in several CFZ samples (Figure 2D). Northern CFZ lavas are more crystal-rich, with 5–10 vol.% euhedral clinopyroxene, 4–8 vol.% subhedral plagioclase and 2–3 vol.% subhedral to anhedral olivine (Figure 2E). A small gabbroic xenolith (11.25 × 5 mm^2) comprising plagioclase and clinopyroxene with minor opaque Fe-Ti oxides is present in one sample. Glomeroporphyritic clusters of clinopyroxene ± olivine ± plagioclase are present in some samples. Macrocryst phases are frequently broken, and exhibit a range of textures including sieve-textured plagioclase cores, and zoned clinopyroxene and olivine cores. Microcrysts of clinopyroxene, plagioclase, olivine, and Fe-Ti oxides are present in varying amounts.

4.1.4 *Monte Brasil (MB)*

The Monte Brasil (MB) group comprises basaltic and trachytic lava and pyroclastic deposits of a remnant Surtseyan tuff volcano forming the southern peninsula of the island [south of Guilherme Moniz; Figure 1b] [Self 1976]. Basalts are porphyritic and dominated by euhedral clinopyroxene (18–32 vol.%) macrocrysts (1–3 mm long axis) and rare megacrysts (≤ 15 mm, Figure 2F). Olivine macrocrysts (2–14 vol.%) tend to be subhedral to anhedral and often exhibit iddingsite within fractures. Plagioclase macrocrysts are rare (≤ 2 vol.%) but plagioclase is a common microcryst and groundmass phase. Melt inclusions are common in both clinopyroxene and olivine crystals. Macrocrysts are set in a fine-grained microcrystalline groundmass of a similar mineralogy. Felsic material at the same location is dominated by tabular, euhedral alkali feldspar macrocrysts (16–18 vol.%) with microcrysts of biotite and clinopyroxene (1–2 vol.%) set in a fine-grained microcrystalline groundmass made up of feldspars and opaque Fe-Ti oxides.

4.1.5 *Pico Alto Volcano (PAV)*

Samples associated with the Pico Alto volcano comprise a'a and pahoehoe lavas of basalt and hawaiite as well as minor trachyte flows found along the northern to northeastern coast of Terceira, with select samples collected from the southern margin of the PAV (Fig. 1b). Mafic rocks are poorly porphyritic (Figure 2G) with subhedral to euhedral strongly zoned olivine macrocrysts (1–4 vol.%) and subhedral clinopyroxene macro- and microcrysts (< 2 vol.%). Plagioclase feldspar is present as microcrysts and dominates the groundmass mineralogy, in addition to opaque Fe-Ti oxides and, minor clinopyroxene and olivine. Microcrysts of olivine, clinopyroxene, and plagioclase feldspar form glomeroporphyritic assemblages in several samples. Felsic material comprises ignimbrites and trachytic lavas which are exposed along the coast, and consist of an alkali feldspar-dominated assemblage (20–25 vol.%) with euhedral to subhedral alkali feldspar macrocrysts which often exhibit perthitic exsolution, euhedral to subhedral minor aegirine-augite, commonly associated with anhedral Fe-Ti oxides, and rare olivine in a fine-grained hypocrystalline groundmass in which feldspar is the dominant crystalline phase.

4.1.6 *Santa Bárbara Complex (SBC)*

Samples from Santa Bárbara were collected from basaltic through hawaiitic and mugearitic cones and flows, and tra-

chytic flows found both stratigraphically beneath and overlying basalt flows, in addition to explosive pumice deposits. Mafic lavas are porphyritic and dominated by mm-sized plagioclase macrocrysts (8–20 vol.%) with minor subhedral to euhedral olivine (4–7 vol.%) and subhedral to euhedral clinopyroxene (1–3 vol.%), surrounded by a microcrystalline plagioclase-dominated matrix. Melt inclusions were identified in both olivine and clinopyroxene. Plagioclase macrocrysts tend to be strongly zoned and often contain a sieve-textured core, they are frequently fragmented, and plagioclase macrocrysts are often found in clusters. Olivine macrocrysts often exhibit iddingsite within fractures and/or along their rims, and some phenocrysts are embayed. Trachytic lavas from Santa Bárbara (Figure 2H) are porphyritic, with a mineral assemblage dominated by tabular euhedral to subhedral alkali feldspar (35–40 vol.%) with minor aegirine, biotite, and opaque Fe-Ti oxides (< 1 vol.%). The groundmass is characterised by a trachytic texture with similar mineralogy, with minor opaque phases and interstitial glass.

4.2 Whole rock chemistry

Major element data and calculated normative mineralogies (CIPW) for Terceira samples are presented in EA (appendix). All CIPW normative mineralogies were calculated using the method of Kelsey [1965]. The samples have basaltic, trachybasaltic to basaltic trachyandesitic and trachytic compositions based on their SiO_2 and total alkali contents (Figure 3). The SiO_2 content (normalised to 100 wt.%, volatile-free) of mafic and felsic rocks ranges between 46–52 wt.% and 65–69 wt.%, respectively, while total alkalis ($Na_2O + K_2O$) range from 1.7–6.2 wt.% for mafic rocks and from 10.2–11.6 wt.% for trachytes. On the basis of their sodic natute ($Na_2O–2 \geq K_2O$; Le Maitre et al. [2002]), the TB and BTA samples can be further classified as hawaiite and mugearite, respectively. Trachytic samples are exclusively peralkaline (PI > 1), with peralkalinity indices [PI = molar (Na + K) / Al] that range between 1.1–1.4.

The most primitive (i.e. MgO-rich) samples are found at Monte Brasil (MB), where SiO_2 ranges from 46.8–47.5 wt.% and MgO from 11.8–14.4 wt.% (Figure 3). Fissure zone samples show a broad MgO range (11.85–3.16 wt.%) over a narrow SiO_2 range (47.2–49.9 wt.%), and samples from the eastern fissure zone are more primitive than CFZ samples. The PAV basalts contain 3.3–6.7 wt.% MgO and 48.1–51.7 wt.% SiO_2, while PAV trachytes contain < 0.4 wt.% MgO and 66.8–68.3 wt.% SiO_2. Similarly, SBC basalts contain 3.5–4.6 wt.% MgO and 49.2–52.0 wt.% SiO_2, whereas SBC trachytes contain negligible MgO and 65.0–68.9 wt.% SiO_2. No intermediate compositions were sampled; however, literature data reveal a paucity of samples in the range ~54 to ~57 wt.% SiO_2 (Figure 3). The Al_2O_3 content in basalts increases from 11.8–16.7 wt.% as samples become more evolved (Figure 3), while trachyte compositions range from 10.6–14.5 wt.%. Some EFZ samples tend towards more Al-rich compositions, reaching 16.7 wt.% Al_2O_3 at only 7.3 wt.% MgO. Between 14.4 and ~4.5 wt.% MgO, $Fe_2O_3^*$ (i.e. total Fe expressed as Fe_2O_3; Figure 3) increases from 10.7–14 wt.% and CaO decreases from 12.7 to 9.8 wt.%, with a subsequent decrease in the concentration of both oxides at ~4.5 wt.% MgO (Figure 3). Rocks from CFZ, PAV, and CPC are more enriched in P_2O_5 than EFZ and MB rocks (Figure 3), reaching up to 1.8 wt.% for the CPC sample, which is in agreement with the caldera wall sample analysed by Self [1976].

CI (chondrite)-normalised rare earth element (REE) patterns (Figure 4) indicate an overall enrichment in light rare earth elements (REE) relative to heavy REE with La_N/Yb_N [N = CI-normalized] ratios of between 7.72 and 11.46. The most primitive samples (MB) are the least enriched in REE relative to chondrite and show slightly negative to moderately positive Eu anomalies, with Eu/Eu^* = 0.95–1.22 [$Eu^* = (Gd_N + Sm_N)/2$], while trachytes (PAV and SBC) are the most enriched in REE and exhibit distinct negative Eu anomalies (Eu/Eu^* = 0.38–0.63). To further quantify the behaviour of all REE, the polynomial function described by O'Neill [2016] was used in the BLambdaR online application [Anenburg and Williams 2022] to calculate individual parameters, λ_n, that express the behaviour of all REE simultaneously (Figure 4). The variable λ_1 represents the slope of the chondrite-normalised REE pattern, reflecting LREE/HREE fractionation, and covers a relatively narrow range for our samples (λ_1 = 11–14), while λ_2 represents quadratic curvature and becomes more negative from trachytes to basalts. Compatible elements such as Ni (Figure 4), Cr, Sc, and Co show positive correlations with MgO, whereas large ion lithophile elements (LILE) such as Ba (Figure 4), Rb, K, and high field strength elements (HFSE) such as Zr (Figure 4), Nb, Hf, and Ta show an inverse correlation, or perhaps an exponential increase, with MgO. Both Ba and V (Figure 4) increase with decreasing MgO content in the mafic samples, and decrease in the trachytic PAV and SBC samples. To some extent, these decreasing trends mirror those observed for Al_2O_3 and Fe_2O_3. More intermediate compositions (3–5 wt.% MgO) define a separate Ba trend, falling between the basalt and trachyte compositions and increasing with decreasing MgO. Similarly, PAV basalts have lower V contents than samples with the same MgO content and define their own trend, decreasing sharply in V content as MgO decreases.

4.3 Mineral chemistry and zoning patterns

4.3.1 *Olivine*

Olivine crystals are abundant in most samples. Core compositions vary from Fo_{69} to Fo_{90} (Figure 6a), while rims span the range Fo_{52}–Fo_{88} (Figure 6b). We note that olivine rims can be subdivided into three groups peaking at Fo_{60}, Fo_{68} and Fo_{80}. In Figs. 6a and 6b, Fo content is plotted against NiO/MnO, a ratio of a compatible element to an incompatible element that strongly decreases with differentiation [Foley et al. 2013].

The most discriminant features of olivine crystals are the zoning types. As such, we have subdivided olivine crystals into five types, based on their chemical and textural features, illustrated schematically in Figure 5: single-step normal zoning (Type I); progressive normal zoning (Type II); reverse zoning (Type III); multiple (normal to reverse) zoning (Type IV; only one crystal); and multiple (reverse to normal) zoning (Type V). Schematic rim-to-core profiles through each zoning type are also shown in Figure 5, illustrating the compositional gradients throughout.

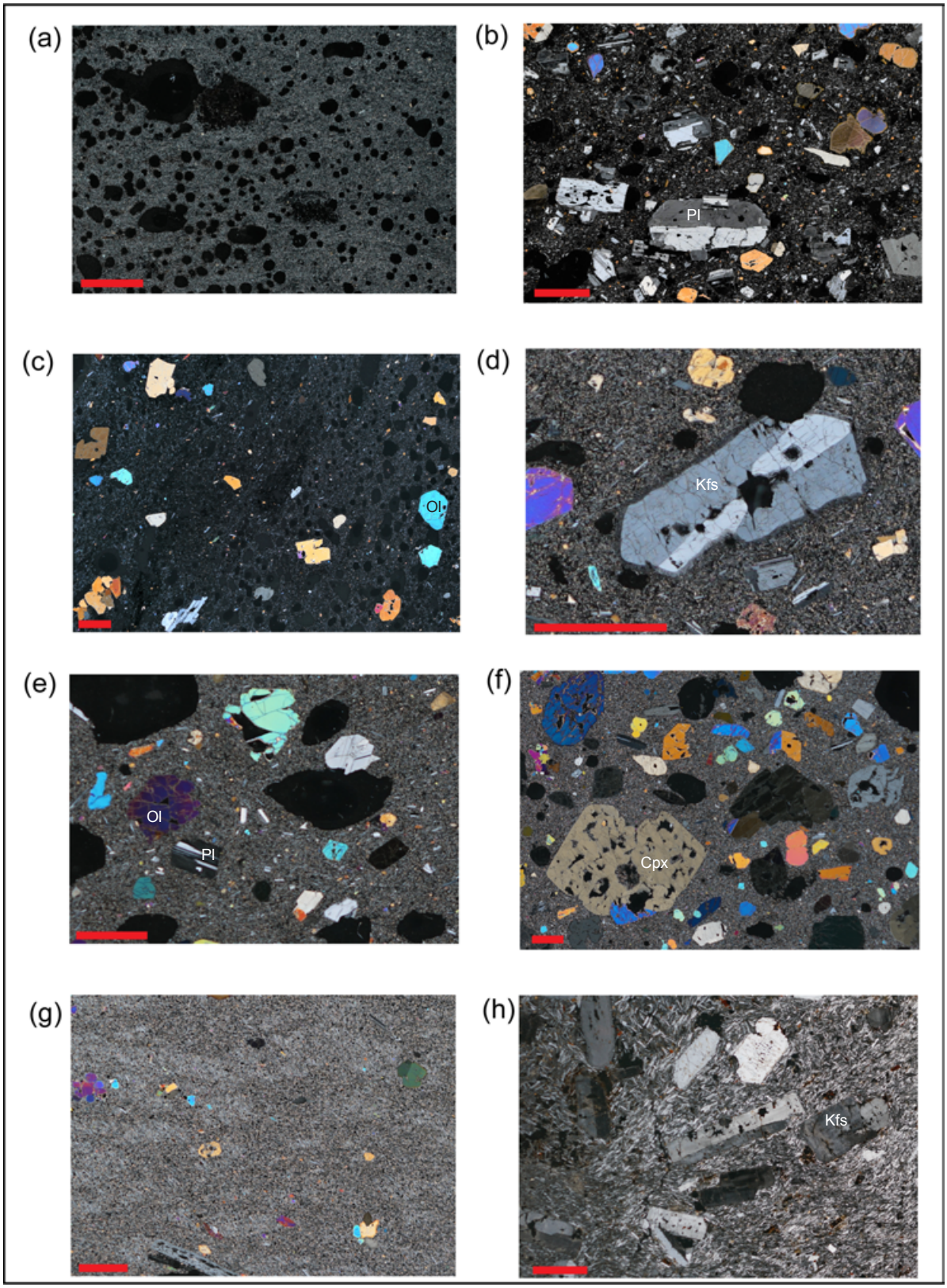

Figure 2: Microphotographs of (a) CPC basalt; (b) plagioclase feldspar-rich EFZ basalt sample; (c) plagioclase-poor vesicular EFZ olivine basalt; (d) rounded alkali feldspar xenocryst with a dark reaction rim in CFZ sample; (e) CFZ basalt with large subhedral olivine macrocrysts, smaller euhedral clinopyroxene crystals and plagioclase feldspar macrocrysts; (f) MB lava with large clinopyroxene macrocrysts and smaller, rounded olivine crystals; (g) poorly-porphyritic PAV hawaiite sample with small olivine and clinopyroxene microcrysts and (bottom edge) sieve-textured plagioclase macrocryst; and (h) alkali-feldspar-dominated trachytic SBC sample. Scale bar = 2 mm. Abbreviations: Pl = plagioclase, Kfs = alkali-feldspar, Ol = olivine, Cpx = clinopyroxene.

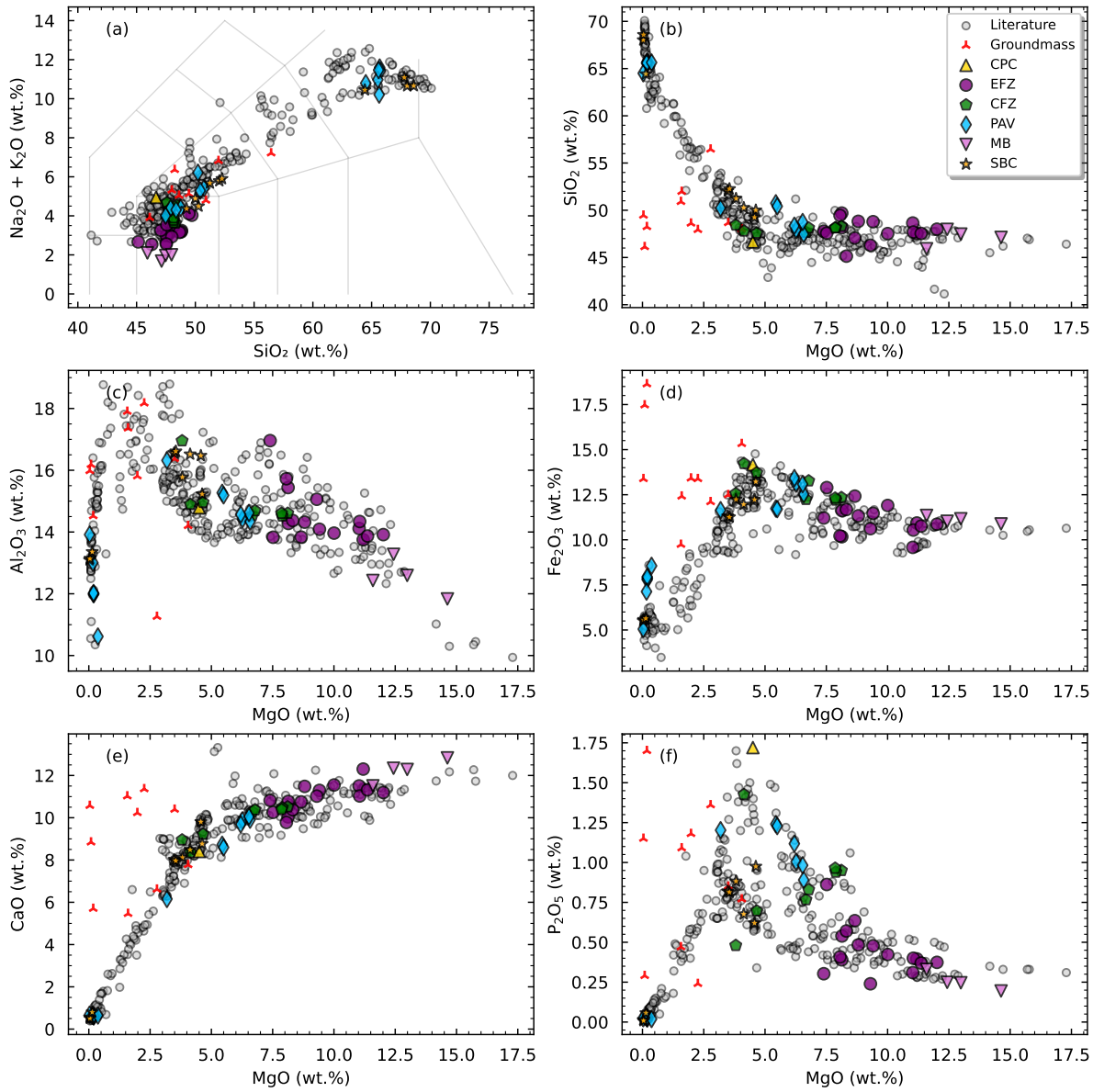

Figure 3: Whole rock compositional data of Terceira samples from the six sample groups: (a) TAS diagram; (b–f) variation diagrams of major elements vs. MgO (wt.%). Coloured regions highlight our samples from each group. Red symbols indicate groundmass glass calculations, discussed later. Solid purple curves indicate the path of fractional crystallisation based on Rhyolite-MELTS modelling. Literature data (grey circles) are from [White et al. 1979], Davies et al. [1995], Mungall and Martin [1995], Beier et al. [2010], Madureira et al. [2011], Madureira et al. [2014], Madureira et al. [2017], Hildenbrand et al. [2014], Zanon and Pimentel [2015] and Pimentel et al. [2016], Jeffery et al. [2017]. Errors (2σ) do not exceed symbol size.

Type I and II cores tend towards the most primitive compositions (Fo_{85}–Fo_{90}), while Type V cores cluster around Fo_{81}. Type III reverse-zoned cores are more evolved, ranging from Fo_{69}–Fo_{83}, and are always more evolved than their rims (Fo_{83}–Fo_{87}). Type I rims have the most evolved compositions, ranging from Fo_{52}–Fo_{78} and NiO/MnO ratios of < 0.5. Combining Ni and Mn, we find that SBC olivine core and rim compositions are characterised by NiO/MnO ratios < 0.6 and < 0.3, respectively. The EFZ and PAV olivines can be divided into cores with high NiO/MnO ratios (1.4–2.7) and both cores and rims with NiO/MnO < 1.6. The relative probability of core and rim compositions (Figure 6c) shows that core compositions fall dominantly between Fo_{82}–Fo_{90}, with a small peak at around Fo_{75} representing the Type III cores, while rim composition peaks fall into three groups: Fo_{61}, Fo_{71}, and Fo_{85}.

4.3.2 *Clinopyroxene*

Clinopyroxenes are subdivided on the basis of their textural and compositional features, illustrated schematically in Figure 7 alongside Mg and Cr WDS maps of example crystals which display different zoning characteristics. Real zoning patterns for major and trace elements are shown in Fig.8, with maps of other crystals presented in Supplementary Figures SF1 and SF2 (Appendix). TOF profiles and regions of inter-

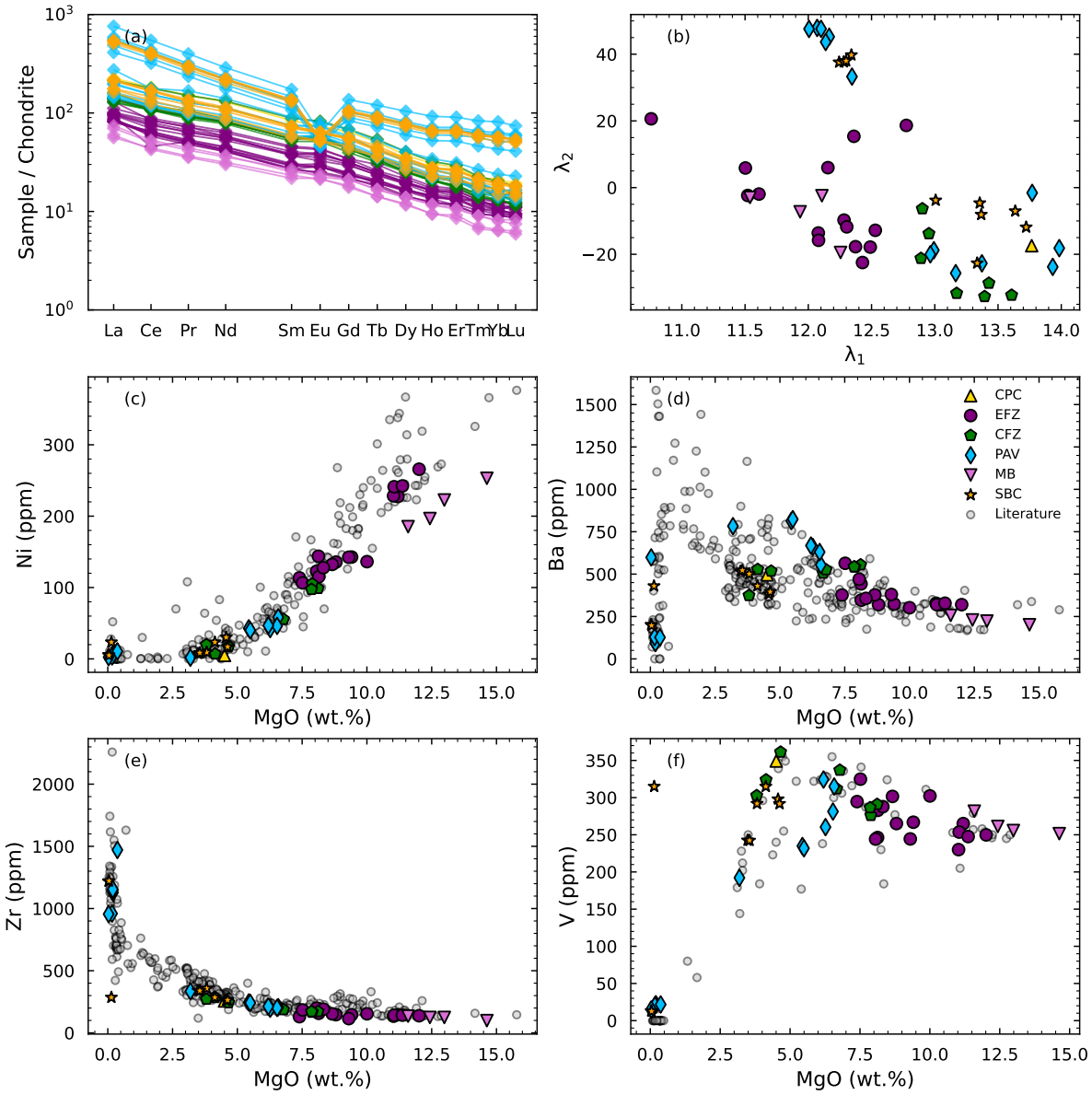

Figure 4: Whole-rock trace element compositional data of Terceira samples from the six sample groups are presented as follows: (a) chondrite-normalised rare earth element (REE) variation diagram [Sun and McDonough 1989], showing that more evolved samples are more enriched in REE relative to chondrite values; (b) REE pattern shape coefficients λ_2 vs. λ_1 for Terceira samples; (c–f) Ni, Ba, Zr, and V (ppm) vs. MgO (wt %) for our samples. Literature data (grey circles) are from the same references as Figure 3.

est (ROIs) were interrogated in greater detail using Cr zoning (e.g. Ubide and Kamber [2018]), which is a highly compatible element in clinopyroxene [Shepherd et al. 2022] (EA and SF3; Appendix). To clearly illustrate the relationship between selected trace elements measured from ROIs, we produced covariance matrices (SF4; Appendix), which show a particularly strong correlation between Cr and Ni. Compositions described below comprise average concentrations of each element within one zoning type, based on results obtained by spot analysis with LA-ICP-MS/MS and elemental mapping via LA-ICP-TOF-MS. The range of Mg# observed in the various sample groups is shown in Figure 9a, where clinopyroxene Mg# is calculated assuming that all Fe is present as Fe^{2+} (e.g. Wieser et al. [2023]).

Type I crystals are defined by their sub-euhedral morphology and low Cr, high Mg, patchy cores (Fig. 7a). Cores and mantles are characterised by irregular crystal domains with variable compositions, identified by dark and light grey areas in BSE images. Type I crystals range between 1000–1300 µm (long axis) and are most frequent in CFZ samples. Core compositions range between Mg# = 80–86; mantles may be slightly more primitive, ranging from Mg# = 81–86, and patchy regions vary on the order of one to two Mg# within each crystal. Rim compositions range between Mg# = 72–81. Element maps, shown in SF1 and SF2 (Appendix) and Fig.8,

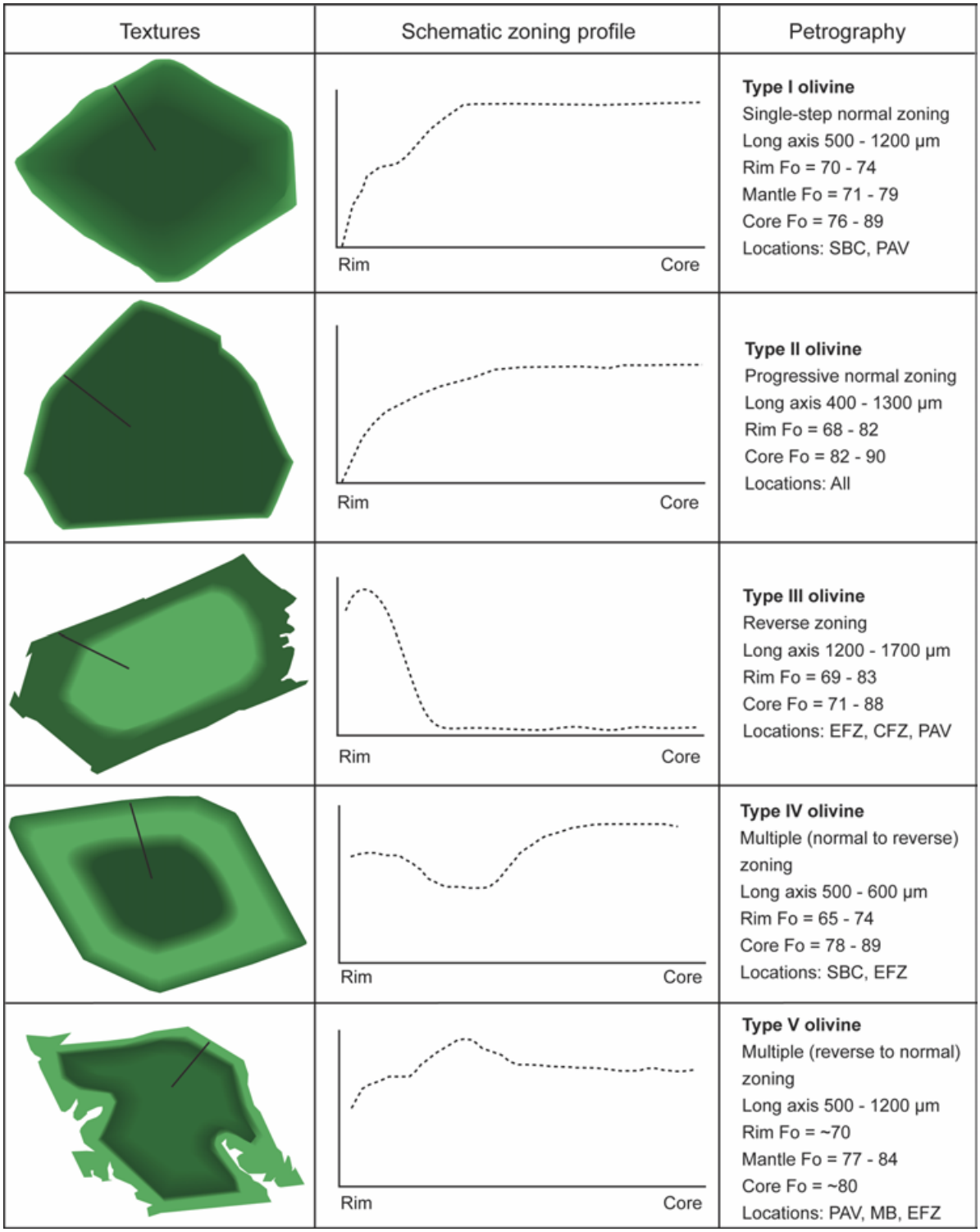

Figure 5: Schematic illustration and petrographical description of the different textures observed in olivine macrocrysts from Terceira basalts alongside rim-to-core profiles that demonstrate the compositional differences between zones.

illustrate the enrichment of Al (and Ti) in lighter (greyscale) patches, while Mg (and Fe) enrichment is apparent in the darker patches. These maps also illustrate that Fe enrichment corresponds to V and REE + Y enrichment, and show a clear, thin band of V, REE + Y, and Zr depletion at the mantle–rim interface in many Type I crystals. Crystal cores are irregular and depleted in Cr (~800 ppm) and Ni (~75 ppm) relative to mantles, which often show coarse Cr oscillations from ~4000 to ~6000 ppm and Ni fluctuations between ~150 to ~200 ppm, reflecting crystal growth during multiple repeated injections of a Ni- and Cr-rich primitive melt, followed by further growth in a subsequently Cr- and Ni-depleted melt.

Type II crystals are characterised by resorbed, anhedral, high-Cr, high-Mg cores (Figure 7b) and range from anhedral,

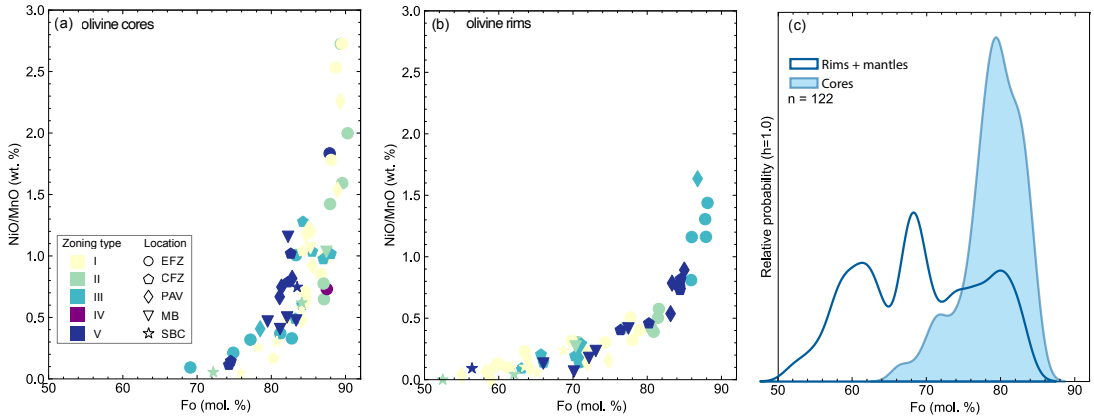

Figure 6: NiO/MnO as a function of forsterite content (Fo = $100 \times Mg/(Mg+Fe)$) in cores (a) and rims (b). Symbols correspond to sample locations, illustrated in the first panel, while colours represent zoning types. (c) Relative probability (bandwidth = 0.77 mol.% Fo) of core and rim compositions from 61 crystals (>120 analyses). 1σ error on Fo is <1 mol.%. 1σ on NiO/MnO is ±0.08. Both errors are slightly smaller than the symbol sizes.

500 µm-long crystals with distinct core and rim regions, to subhedral, 1000 µm-long crystals with core, mantle, and rim regions identified by a significantly darker central region (greyscale BSE), surrounded by light grey mantles and rims. Type II crystals are found in all sample groups except SBC. They have relatively homogeneous core compositions (Mg# = 79–92), with a sharp transition to a more evolved mantle (Mg# = 78–88) and rim (Mg# = 69–80). Element maps show that the crystal cores are enriched in Cr (~7000 ppm, some reaching 10,000 ppm), Ni (~200 ppm), MgO, and variable amounts of Al_2O_3, relative to mantles (Cr ~4500 ppm, Ni ~125 ppm) and rims (Cr ~1200 ppm, Ni ~100 ppm), while mantles and rims store a higher concentration of REE + Y (~10 ppm) and V (~300 ppm). One of the Type II PAV crystals identified is reversely zoned, with a more primitive rim (Mg# = 78) and a more evolved core (Mg# = 76), and contains 942 ppm Cr and 12.15 ppm Ce, more indicative than other Type II rim compositions.

Type III crystals include crystals with sector zoning, oscillatory zoning, or a combination of both (complex zoning) (Figure 7c). Sector zoning in clinopyroxene is characterised by hourglass {111} sectors that often diverge from equilibrium compositions, and prism {hk0} sectors that can approach equilibrium compositions [Neave et al. 2019; Ubide et al. 2019b]. The hourglass and prism sectors can be identified in plane-polarised light or by differences in BSE intensity. Hourglass sectors are enriched in SiO_2 (>50 wt %) and MgO (>15 wt %) relative to Al and Ti, while prism sectors are enriched in Al_2O_3 (>5 wt %) and TiO_2 (>1.5 wt %). Prism sectors are also enriched in Cr (4000–5000 ppm), V (~300 ppm), Sc (~100 ppm), and REE (Ce = 6–10 ppm) relative to hourglass sectors (Cr ~3000 ppm; V ~200 ppm; Sc ~78 ppm; Ce = 4–6 ppm). Oscillatory zoning describes concentric bands of higher and lower element concentrations, with oscillations in Fe, Mg, and Cr (on the order of up to 3000 ppm; SF4; Appendix), as well as Al, being especially pronounced. Sector- and oscillatory-zoned crystals are most frequent in EFZ samples, with some CFZ and few PAV and SBC sample groups containing Type III crystals.

Type IV crystals (Figure 7c) originate mostly from MB and CFZ and are characterised by an abrupt core/rim boundary, identifiable by a thin (20–50 µm) lighter grey rim around the edge of the crystal and a darker, generally homogeneous core with no apparent intermediate region, indicative of two stages of growth. Type IV crystals tend to be subhedral to anhedral, often embayed, and range in size from 500–1100 µm. Core compositions range from Mg# = 79–88, and rims fall within the range Mg# = 74–83. Rims are enriched in Al_2O_3 (5.3–6 wt%) and TiO_2 (1.5–3.3 wt%), relative to cores (4 and 1.5 wt% respectively), while cores are enriched in MgO (14.7–15.3 wt%) and Cr_2O_3 (0.3 wt%) relative to rims (12.7–14 wt% and <0.1 wt% respectively). Sample T38_px_01 was the only Type IV crystal analysed for trace elements and is characterised by a rim enriched in V (500 ppm), Zr (33 ppm), and REE + Y (Ce ~11, Y ~16) and depleted in Cr_2O_3 (Cr ~170 ppm) and Ni (80 ppm) relative to its core.

4.3.3 *Plagioclase*

We distinguish four types of plagioclase crystals based on zoning patterns and morphology, illustrated in Figure 10. Type I plagioclase crystals (Figure 10a) range from 1 to 2.1 mm (long axis), are subhedral and frequently embayed, and exhibit fine- to coarse-scale (<10 µm and 20–50 µm width bands) oscillatory zoning from mantle to rim, with typically unzoned cores. Oscillatory bands are often wavy, indicating resorption [Van Gerve et al. 2020]. Core compositions are relatively homogeneous and range from An_{60-64} between samples, rims are generally An_{59-60}, and oscillatory bands fluctuate between An_{54-64}, with higher-An higher-An bands (An_{73-75}) in several crystals.

Type II plagioclase crystals are 0.7–2 mm (long axis) and subhedral to euhedral, with distinct core and rim compositions (Figure 10b) characterised by high-Ca cores (An_{75-86}) and lower Ca-rims (An_{51-73}). Rim thicknesses are variable but span the range 10–40 µm. Some Type II crystals may have one to two bands in their mantles between An_{70-75}.

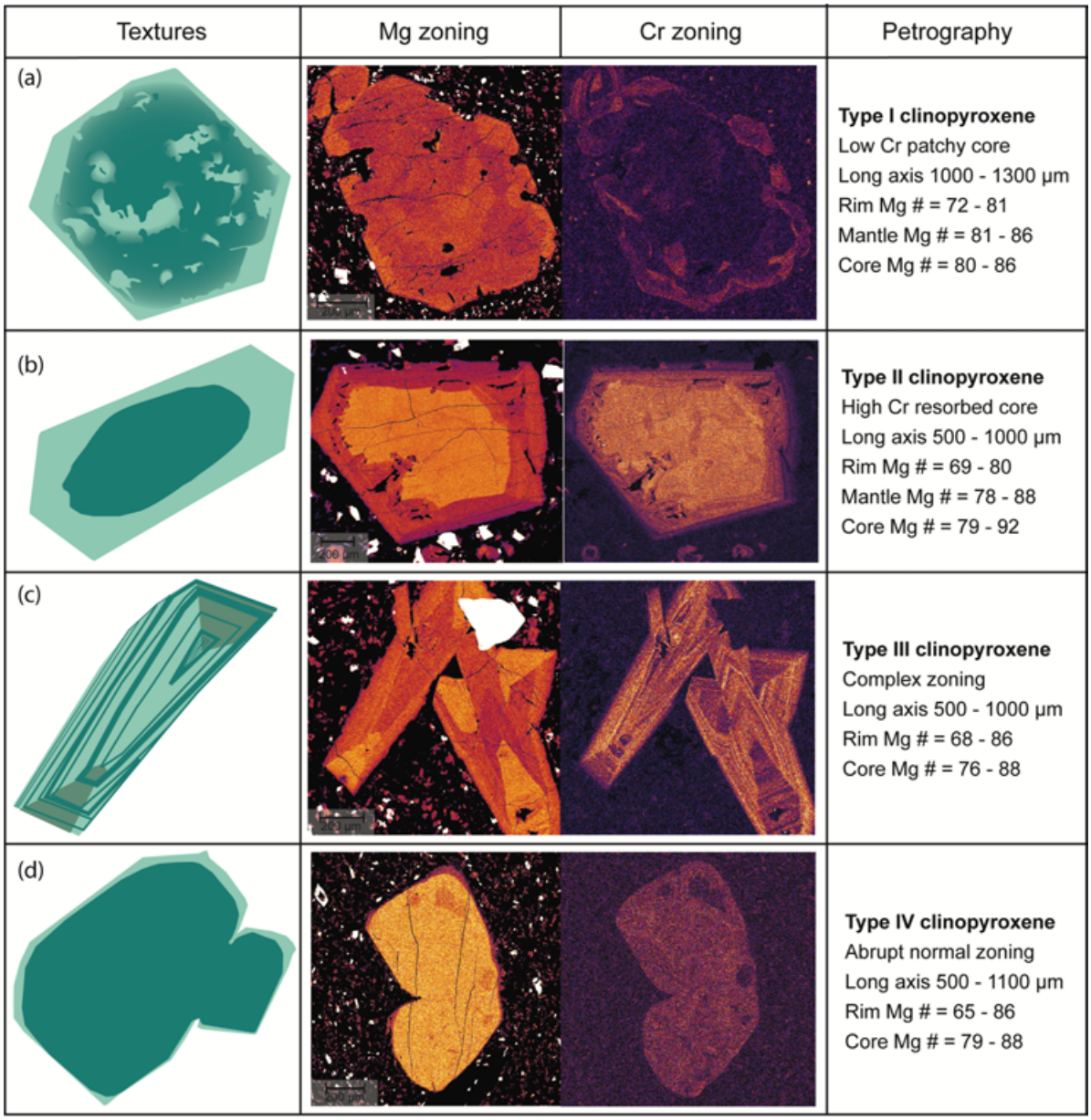

Figure 7: Schematic illustrations of clinopyroxene textures illustrated alongside Mg and Cr maps of representative crystals from each zoning type (a) Type I, (b) Type II, (c) Type III, (d) Type IV and a brief petrographic description.

Type III crystals (Figure 10c) are characterised by sieve-textured, high-Ca cores (An_{77-83}) and low-Ca rims (An_{47-60}), and range in size from 0.8 to 2.5 mm.

Type IV plagioclase are the largest crystals, ranging in size from 1.7 to 3 mm and exhibit strong oscillatory zoning from core to rim (Figure 10d). Cores tend to exhibit an inhomogeneous, patchy texture with various distorted bands and regions of varying An content, while mantles and rims tend to exhibit clearer oscillatory zones of varying thickness. They are often found in association with other Type IV plagioclase crystals and clinopyroxene crystals or Fe-Ti oxides in glomeroporphyritic assemblages. Zones fluctuate in composition from An_{57-85}.

Plagioclase and clinopyroxene core and rim compositions tend to correlate within sample groups, exemplified in Figure 9, which shows the range in clinopyroxene Mg# (Figure 9a) and plagioclase An content (Figure 9b) for each sample group. Measured alkali feldspar xenocrysts characterised by low An contents (An_{5-19}) are also included in Figure 9b.

4.3.4 *Fe-Ti oxides*

Magnetite and ilmenite microcrysts are found only in EFZ, CFZ, PAV, and SBC samples, while spinels are found in association with olivine, and less frequently with clinopyroxene, in EFZ, CFZ, PAV, SBC, and MB samples. Ilmenite crystals are almost pure ilmenite (Ilm_{77-93}; calculated using Andersen and Lindsley [1985]), with minor proportions of geikielite (Gei_{4-21}) and less than 1 % hematite. Magnetites fall on the ulvöspinel side of the ulvöspinel–magnetite solid solution (SF5; Appendix), ($Mt_{10-30}Usp_{69-90}$). The EFZ spinels fall mainly in the Al-chromite to Fe-chromite field, while CFZ samples span

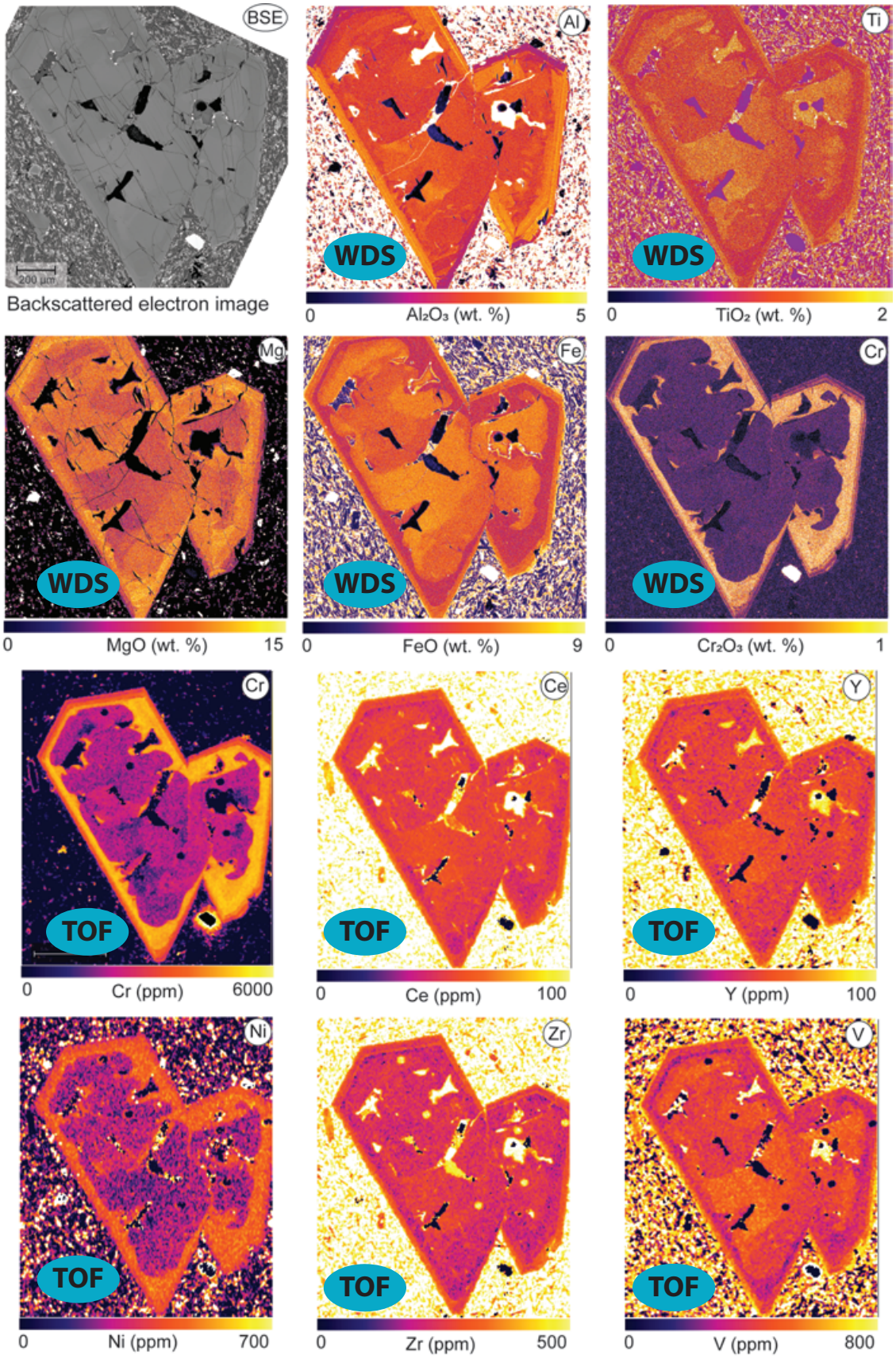

Figure 8: Major and trace element maps of T14_px_08, a Type I clinopyroxene, illustrating zoning patterns obtained from WDS (Al, Ti, Fe, Mg, Cr, wt.%) and TOF (Cr, Ce, Y, Ni, Zr, V, ppm); note that Cr was analyzed using both methods.

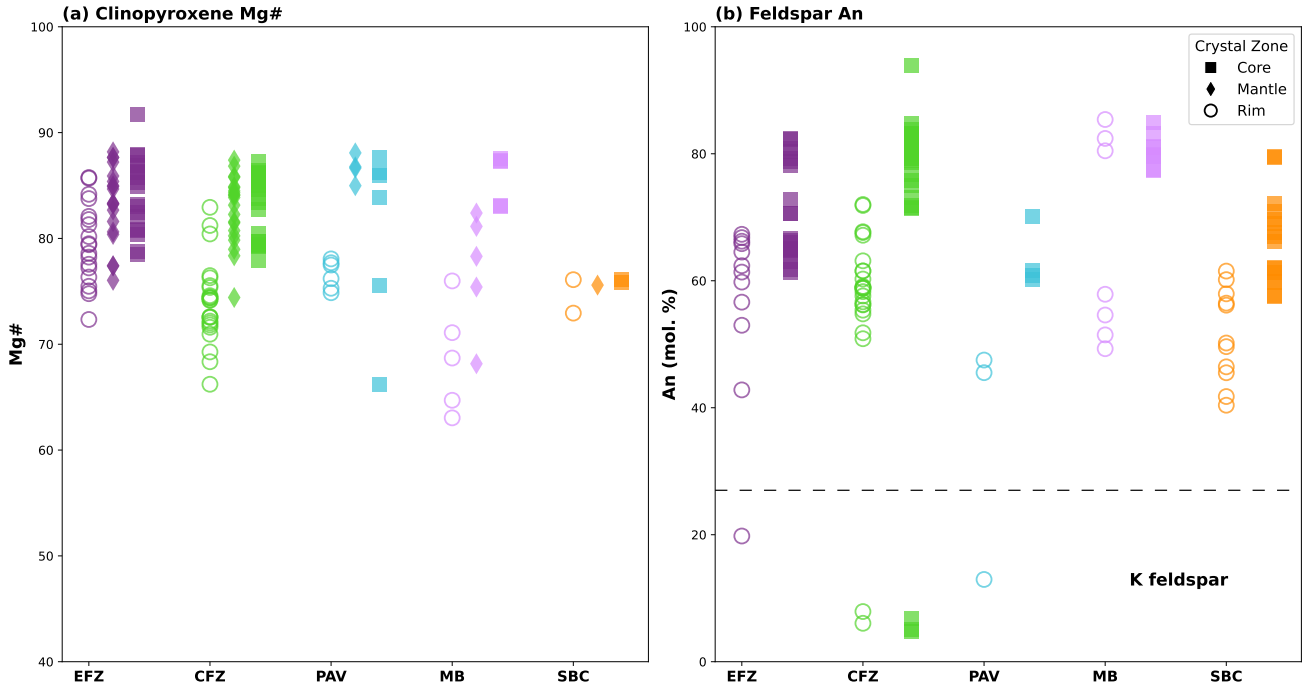

Figure 9: Range in (a) clinopyroxene Mg number and (b) plagioclase anorthite content for cores, rims and mantles (clinopyroxene only) for each sample location.

a range of compositions from Al-chromite through picotite to Fe-picotite.

In terms of major element compositions, the TiO_2 content of the Fe-Ti oxides ranges from 46.68 to 52.30 wt.% (ilmenite), 12.45 to 25.99 wt.% (magnetite), and 0.93 to 14.42 wt.% (spinel), while the FeO + Fe_2O_3 contents range from 43.44 to 48.82 wt.% (ilmenite), 62.74 to 74.32 wt.% (magnetite), and from 26.15 to 58.05 wt.% (spinel).

5 Discussion

5.1 Crystal-melt equilibrium conditions

The absence of groundmass glass and quenched, glassy, melt inclusions prevents direct measurement of melt compositions in Terceira lavas. We therefore approximate groundmass compositions as proxies for melt composition by mass balance using bulk-rock compositions and representative mineral compositions measured by EPMA and EDX. We note that the size threshold we use between matrix (quenched) crystals and phenocrysts Zellmer [2021] might affect the results of our calculations of matrix compositions. However, we believe that this is insignificant for the samples we chose which contain few crystals with intermediate size; i.e. they are either very small and classified as groundmass or large and classified as macrocrysts (or megacrysts). Following the approach of D'Mello et al. [2023], we calculated groundmass compositions using the following equation:

$$C_{\mathrm{GM}} = \frac{C_{\mathrm{WR}} - XC_{\mathrm{MIN}}}{1 - X} \quad (5)$$

Where C_{GM} = groundmass composition (wt.% oxide), C_{WR} = whole-rock composition (wt.% oxide), C_{MIN} = average mineral assemblage composition (wt.% oxide) and X = proportion of crystals. We performed groundmass mass balance calculations on a total of ten representative samples, listed in EA (Appendix). In brief, we calculated C_{MIN} by multiplying the composition of each mineral (wt.% oxide) by its proportion within the lava and adding up the totals. Mineral phase compositions and proportions used to calculate C_{MIN} are listed in EA (Appendix). The calculated groundmass compositions are illustrated in Figure 3 and are slightly more evolved than whole rock compositions with 46–56 wt.% SiO_2. Samples with higher proportions of olivine result in groundmass compositions with MgO contents 80% lower than whole-rock compositions, reflecting the effect of olivine accumulation on whole rock compositions, while plagioclase-rich samples contain up to 50% less CaO in the groundmass. Groundmass compositions contain more TiO_2 than the whole rock, up to 50% in some cases, which we attribute to a high concentration of Ti-bearing phases such as Fe-Ti oxides in the groundmass and small oxides that were missed during point counting. Many calculated groundmass compositions have low Mg# and cannot be in equilibrium with the crystals which they carry. Further insights can be gained by determining whether the crystal cargoes of our samples are in equilibrium with their whole-rock hosts and thus evaluating the extent to which whole-rock composition (i.e. groundmass and crystal mixtures) represent true magmatic liquids.

Chemical equilibrium between clinopyroxene and whole-rock compositions was assessed using the Fe-Mg exchange equilibrium range ($Kd^{\mathrm{Fe\text{-}Mg}}_{\mathrm{cpx\text{-}melt}}$; Putirka [2008]) in which all Fe in clinopyroxene crystals and whole-rocks is assumed to be Fe^{2+}) and the ΔDiHd test following Putirka et al. [1996]

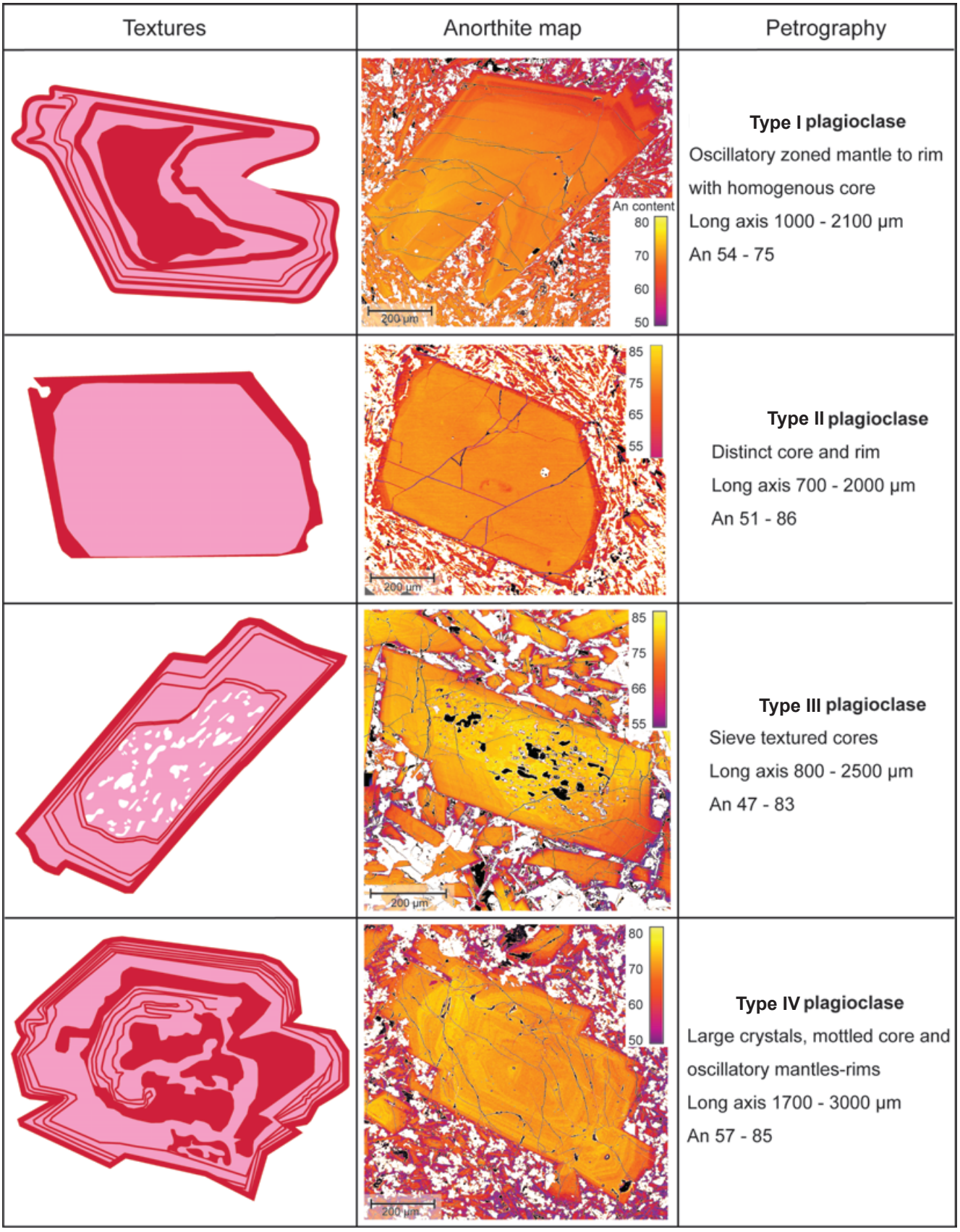

Figure 10: Schematic illustrations of plagioclase textures and calibrated anorthite maps of representative crystals in each population.

and Mollo et al. [2013]. Equilibrium was assumed when $Kd^{\text{Fe-Mg}}_{\text{cpx-melt}} = 0.28 \pm 0.08$ [Putirka 2008] and ΔDiHd (diopside and hedenbergite components observed in the analysed crystals vs. those predicted from melt compositions) approached zero [Mollo and Masotta 2014]. Most clinopyroxene rims are not in equilibrium with their whole-rock hosts (Fig. 11) and tend to have lower Mg# than would be expected to fall within the equilibrium range (Figure 11a); these lower Mg# contents are, however, likely to be in equilibrium with the more evolved groundmass compositions calculated above. Cores and mantles from CFZ and EFZ basalts are frequently in equilibrium with whole-rock hosts, while PAV cores and mantles tend to have higher Mg# values than expected for equilibrium (i.e. they are more primitive than their whole-rock hosts). Less discrepancy between sample groups is apparent in the DiHd predicted vs. observed diagram (Figure 11b); however, it is clear that the majority of the core, rim, and mantle compositions have higher DiHd values than predicted. Altogether, this supports that clinopyroxenes are dominantly in chemical disequilibrium with the whole-rock composition in which they are found.

The equilibrium crystallisation conditions of olivine were modelled through the Fe–Mg exchange reaction using equations 8a and 8c of [Putirka 2016]. Equilibrium was assumed when $Kd^{\text{ol–melt}}_{\text{Fe–Mg}} = 0.30 \pm 0.03$ [Roeder and Emslie 1970]. An $Fe^{3+}/\Sigma Fe$ ratio of 0.22 was used for the Kd calculation, reflecting redox conditions of around 0.75 log units above fayalite-magnetite-quartz (FMQ) equilibrium, similar to the redox conditions determined for the Canary Islands by Moussallam et al. [2019] and in line with recent calculations performed on nearby Pico [van Gerve et al. 2024]. This is also in agreement with Fe-Ti oxide oxybarometry (see below). Olivine compositions from Terceira, shown in Figure 12a, are predominantly out of equilibrium with the whole rock: our models highlight that about 75% of olivines are out of equilibrium with their host. For the olivines that are in equilibrium, whole rock compositions range from Mg#58–68 (cores) and Mg#40–62 (rims), and forsterite contents from Fo_{82-87} (cores) and Fo_{68-84} (rims). There is no clear correlation between equilibrium conditions and zoning type (colour scale) for olivines.

Plagioclase equilibrium conditions were tested through the Ab–An exchange reaction [Putirka 2008], in which the equilibrium constant is constrained within high-temperature (> 1050 °C, $Kd^{\text{plag–melt}}_{\text{Ab–An}} = 0.27 \pm 0.11$) and low-temperature (< 1050 °C, $Kd^{\text{plag–melt}}_{\text{Ab–An}} = 0.10 \pm 0.05$) intervals. Our estimates (Figure 12b) indicate that most core compositions correspond to the equilibrium range of $Kd^{\text{plag–melt}}_{\text{Ab–An}} = 0.27 \pm 0.11$, however, some of the most primitive CFZ plagioclase cores (An_{81}–An_{85}) are out of equilibrium with the whole-rock compositions. Around half of the PAV and EFZ cores are out of equilibrium with the host, while the remaining half fall within the equilibrium range. Most rim compositions are out of equilibrium with the host.

In summary, our analysis indicates that the majority of crystals observed in Terceira lavas are not in thermodynamic equilibrium with either the whole-rock composition or the estimated composition of their carrier melt, derived from the calculated groundmass. This suggests that most crystals represent antecrystic material – crystal cargo originating from disaggregated crystal mushes that were entrained and transported to the surface during eruptive events [Humphreys et al. 2025].

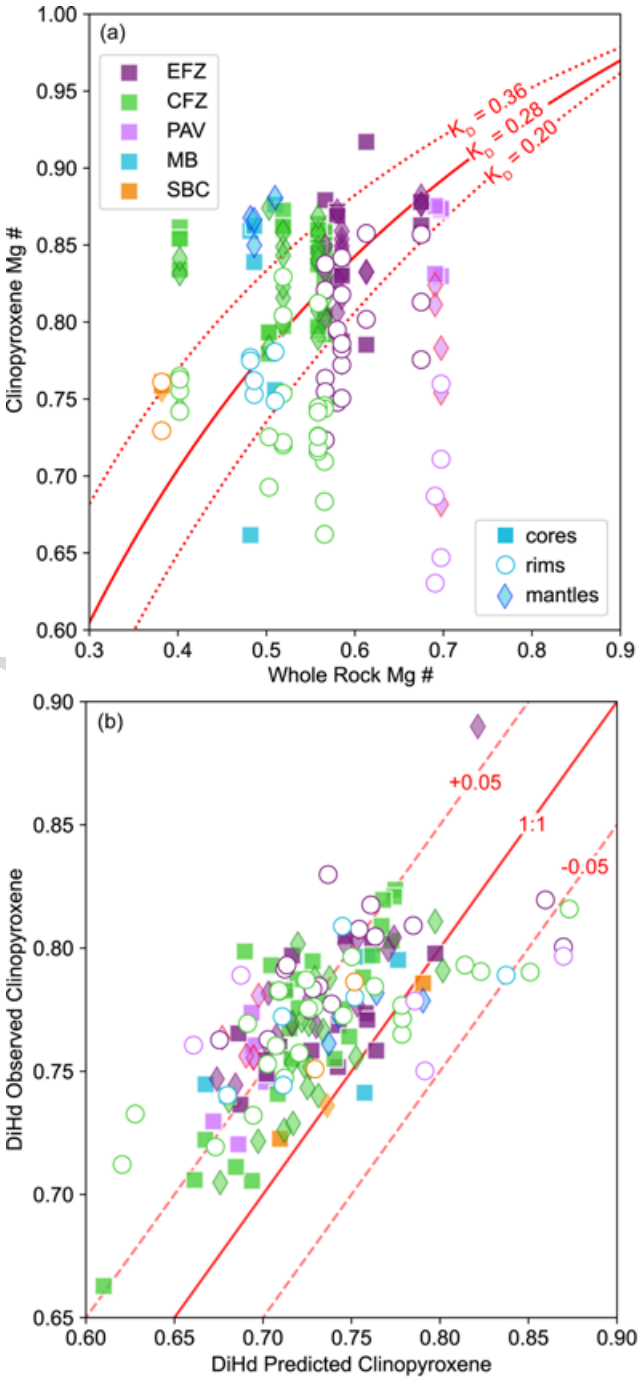

Figure 11: Tests for equilibrium between clinopyroxene and whole rock based on (a) the Fe-Mg exchange reaction $Kd^{\text{Fe-Mg}}_{\text{cpx-melt}}$ [Putirka 2008] and (b) the thermodynamic expression for diopside + hedenbergite (ΔDiHd)[Mollo et al. 2013].

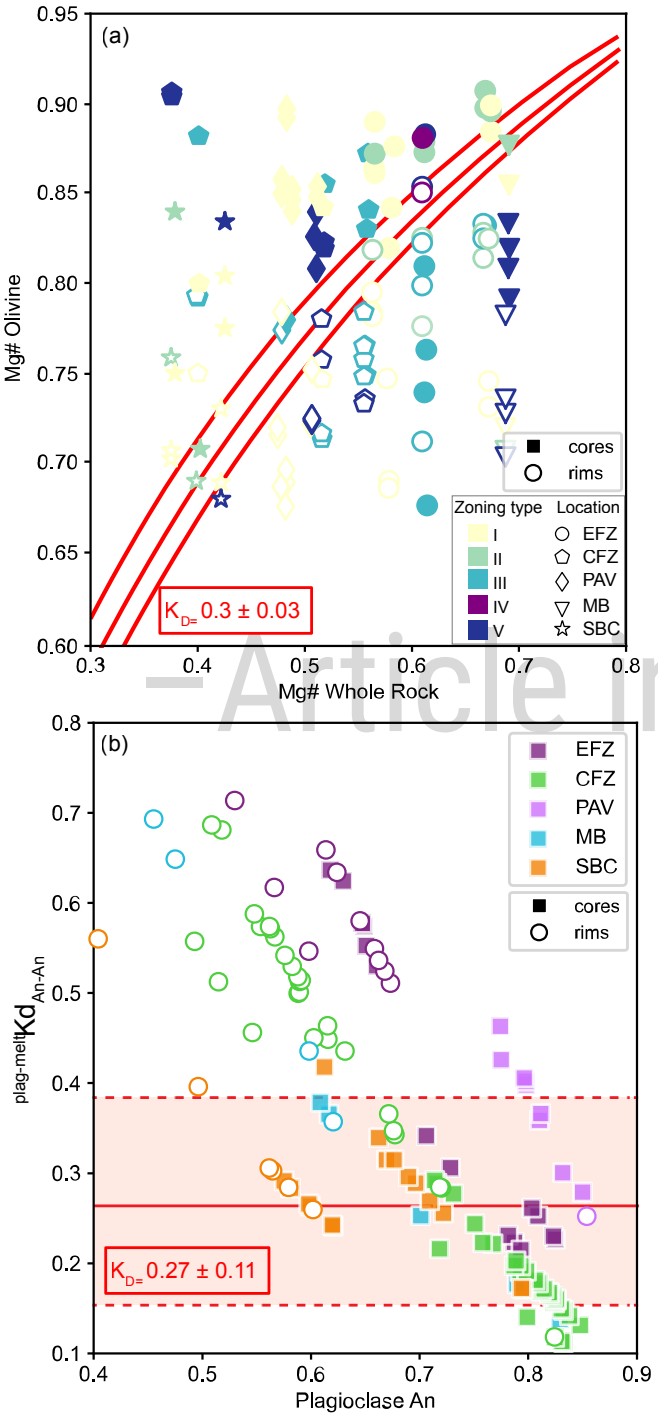

Figure 12: Test for equilibrium between (a) olivine and whole rock based on the Fe–Mg exchange reaction of Roeder and Emslie [1970]; (b) plagioclase and melt based on the Ab–An exchange reaction of Putirka [2008].

5.2 Origin of clinopyroxene crystal zoning patterns

Patchy, diffuse zones of Fe–Mg enrichment and Al–Ti depletion, and Fe–Mg depletion and Al–Ti enrichment in Type I clinopyroxenes are interpreted to reflect the introduction of new magma into the magma reservoir, changing the physicochemical properties of the melt and resulting in dissolution-recrystallization textures [Streck 2008]. The Cr-poor cores, however, suggest that the early magmatic environment that experienced magma recharge was fundamentally distinct in composition from the recharge magmas that produced the surrounding Cr-rich rims. Patchy or corroded zones of element enrichment in Type I crystals may also represent older crystals originating from colder storage zones close to or below the solidus temperature that experienced repeated interactions with batches of mafic magma [Cooper and Kent 2014].

Resorbed cores characteristic of Type II clinopyroxenes may represent dissolution features or remobilised antecrysts originating from a compositionally different region of the plumbing system that experienced resorption during ascent and grew further in a Cr- and Ni-rich, newly injected, hot magma (e.g. Stromboli; Di Stefano et al. [2020] and Petrone and et al. [2022]). During (adiabatic) ascent, crystals are resorbed as a result of superheating relative to the liquidus and changes in mineral stability [Annen et al. 2006; Neave and Maclennan 2020]. Crystals or cumulate fragments (e.g. Turner et al. [2003]) that were entrained in an ascending magma likely underwent continued fractionation, convection, cooling, and mixing with new, hotter magma batches (e.g. Humphreys et al. [2006]), resulting in thermal erosion of the older core over time. High-Cr resorbed cores imply that the crystals originated from a deeper, more primitive melt, perhaps originating directly from a mantle source Jorgenson et al. [2024], rich in Cr and Ni, while a more evolved upper reservoir depleted in Cr and Ni gave rise to the more evolved rim compositions in Type II crystals. Type II clinopyroxene crystals are found only in PAV and MB lavas, suggesting that there may potentially be a subvolcanic link between the two volcanic centres.

Hourglass and prism sectors in Type III clinopyroxenes form in response to the interplay between crystallographic controls on the mineral, such as the preferential uptake of elements in crystal faces with different arrangements of the T, M1, and M2 sites [Nakamura 1973; Mollo and Hammer 2017], and kinetic effects during cooling and crystallisation. Charge balance mechanisms control the distribution of elements in the clinopyroxene crystal structure [Ubide et al. 2019b]; cations with a high charge and small ionic radius (i.e. high field strength elements (HFSE)) are more firmly bonded to the structural sites of Al-rich prism {100} sectors in M1 sites, while trivalent rare earth elements (REE) + Y predominantly reside in M2 sites. Furthermore, sector-zoned pyroxenes are commonly associated with alkaline melts such as Azorean basalts [Wass 1973; Leung 1974; Self and Gunn 1976; Neave et al. 2024], in which Al plays a dominating role, giving rise to prominent Al- and Ti-rich zones [Downes 1974]. Experimental data demonstrate that sector zoning can develop when the extent of crystal growth exceeds the rate of lattice diffusion [Downes 1974; Leung 1974; Watson and Liang 1995], and that sector zoning is strongly controlled by the degree of magma undercooling and, in turn, by the rate of crystal growth [Kouchi et al. 1983]. For clinopyroxene crystals to grow to the large macrocryst sizes frequently observed in Terceiran basalts, a certain amount of undercooling ($\Delta T = T_{\text{liquidus}} - T_{\text{crystallisation}}$) is required [Kirkpatrick et al. 1981]. However, Ubide et al. [2019b] demonstrate that sector zoning can develop under near-equilibrium conditions at relatively low degrees of un-

dercooling (ΔT = 13–18 °C) and slow growth rates in their study of Etnean lavas. As such, the presence of both large and sector-zoned clinopyroxene crystals in Terceiran basalts suggests that magmas experience low but non-negligible degrees of undercooling and, by extension, slow crystal growth rates.

Oscillatory zoning in magmatic minerals if often explained by either extrinsic mechanisms that involve changes in the physicochemical properties of the bulk system, linked to processes such as magma replenishment, convection, and fluid mixing, or by intrinsic mechanisms that involve coupling between the rate of crystal growth and element diffusion through the crystal-melt boundary layer [Shore and Fowler 1996; Ginibre et al. 2002]. In this case, the growing crystal is surrounded by a narrow boundary layer that becomes depleted in certain growth constituents compared to the bulk liquid. The interplay between the crystal growth rate and the diffusion of elements across this advancing boundary layer leads to chemical oscillations within the crystal. Fine-scale Cr oscillations in Type III clinopyroxenes, such as the ~5–8 µm bands observed in `T54_px_06` (Fig. 13), may reflect minor fluctuations in pressure, temperature, and melt composition during convection [Elardo and Shearer 2014], or may result from boundary layer effects. In contrast, the coarser oscillatory zoning of 25–50 µm in `T14_px_06` and 60–120 µm in `T37_px_01` is more likely associated with magma replenishment events [Ubide et al. 2019b; Schoneveld et al. 2020]. The shape of these oscillations, deduced from the WDS and TOF maps, indicates both sharp and diffuse oscillations. Sharp, euhedral Cr oscillations may indicate minor changes in intensive or extensive parameters through time, though they more likely reflect crystal convection within a heterogeneous magma reservoir (e.g. Ubide et al. [2019a]). Diffuse and jagged boundaries between Cr oscillations indicate resorption and crystal–melt disequilibrium, suggesting substantial changes in the pressure, temperature, and/or composition of the magma reservoir due to mafic magma replenishment [Downes 1974; Perugini et al. 2005; Ginibre et al. 2007].

Zoning in Type IV crystals is characterised by Cr-, Ni-, and Mg-rich cores and mantles with sharp transitions to Fe-, Ti-, and Al-rich rims. This abrupt zonation is most likely related to two growth stages [Schoneveld et al. 2020]. Specifically, the mafic core is likely to represent open-system growth in a freely convecting, near-liquidus temperature magma, where growing crystals and their host melts maintain equilibrium conditions. In contrast, the more evolved rim may represent a second stage of crystal growth after transport to another, more evolved, perhaps shallower, part of the plumbing system [Van Gerve et al. 2020].

Type I clinopyroxene crystals with low-Cr resorbed cores and high-Cr mantles and rims are found only in CFZ samples, while Type IV crystals with low-Cr cores and moderate-Cr rims span both the EFZ and CFZ, implying that the products from the fissure zone tap a low-Cr, more mature reservoir, while the central region of the fissure zone benefits from an influx of more Cr-rich, primitive magma. This is consistent with the evolution of the island of Terceira in general, whereby a west-to-east decrease in the age of eruptive units correlates with an increase in activity [Self 1976; Calvert et al. 2006; Nunes et al. 2014]. Type III crystals that exhibit oscillatory and/or sector zoning are most abundant in EFZ clinopyroxenes, though examples are also found in PAV and SBC clinopyroxenes. This suggests a dynamic reservoir with low undercooling and multiple recharge events from a more primitive, Cr-rich magma. The only example of reverse-zoned clinopyroxenes is found in an EFZ sample, further supporting the idea of a complex, multi-layered plumbing system in which the rims are more likely in equilibrium with the primitive, Mg-rich intruding magma.

5.3 Pre-eruptive magma storage conditions

Temperature and oxygen fugacity estimates of the pre-eruptive conditions of Terceira were obtained from two-oxide equilibria in basalts. While Fe-Ti oxides are often present in the groundmass of Terceiran basalts, finding coexisting ilmenite and magnetite of sufficient size for chemical analysis proved difficult. Where we were able to measure coexisting Fe-Ti oxides, magnetite and ilmenite pairs occurring in the same rock samples that pass the Mn–Mg equilibrium test yield a range of fO_2 conditions from 0.5 log unit below FMQ to just one log unit above FMQ (Fig.13), and a temperature range between 899 °C and 1256 °C. SBC samples record the largest range in both temperature and fO_2 conditions.

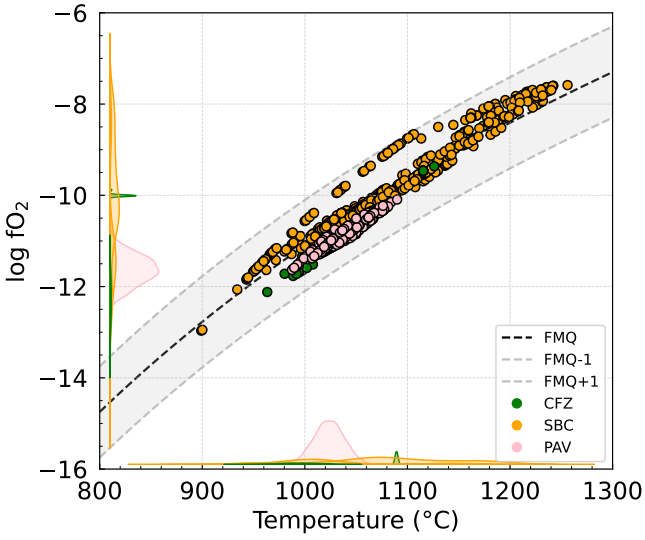

Figure 13: Results of two-oxide thermometry determined for magnetite-ilmenite pairs. Density distributions on the x and y axes are calculated for individual samples.

Insights into magma storage conditions can be obtained from clinopyroxene crystallisation temperatures and pressures. Single-phase thermobarometers can theoretically capture the crystal's entire growth history, revealing the full range of P–T conditions in trans-crustal magmatic systems. We thus performed clinopyroxene-only thermobarometry using the iteration of equations 32b and 32d of Putirka [2008], and the machine-learning-based thermobarometer of Jorgenson et al. [2022], i.e. models P08, and J22 (Fig.14, Figure 15). Calculated temperature generally overlap with those obtaiened from Fe-Ti oxide thermometry (SF6; Appendix). We note that mineral-only thermobarometers have been suggested to un-

derestimate pressure relative to traditional mineral–melt thermobarometers. For example, Ubide et al. [2023] systematically compared P–T estimates derived from clinopyroxene-only machine-learning models with those obtained from equilibrium clinopyroxene–melt pairs. No current thermobarometers are sufficiently precise to resolve small, distinct reservoirs within the crust due to their uncertainties typically exceeding 100–200 MPa, though thermobarometric results may be considered in conjunction with textural data to constrain crystallisation conditions in the upper and lower crust.

The clinopyroxene-only thermobarometer of Putirka [2008] requires an estimate of magmatic H_2O. We assume a H_2O content of 0.5 wt% based on prior fluid inclusion measurements [Zanon and Pimentel 2015], but realistically this value will not be the same for every melt pocket. The model allows uncertainties to be quantified for each individual clinopyroxene composition, rather than across entire suites of analyses. Error bars in Fig.14 reflect different estimates of uncertainty from each of the three models: uncertainties on model P08 are reported as 87 °C and ±260 MPa [Putirka 2008]; uncertainties on estimates from model J22 are assessed on the basis of the interquartile range (IQR) of voting distributions from each random forest, as suggested by Jorgenson et al. [2022]. With these models, we record pressure conditions from the MOHO or slightly higher (~ 500-600 MPa) to the sub-surface. The estimated pressure and especially temperature conditions derived from the matched clinopyroxene–melt pairs overlap with those obtained from the mineral-only thermobarometer, indicating that the application of the mineral-only model to the Terceira samples is justified.

Uncertainties in our thermobarometric calculations mean that these estimates are most reliably interpreted when integrated with independent *P–T* constraints and textural observations. For example, Zanon and Pimentel [2015] determine magma ponding depths of 498–575 MPa, with central lavas experiencing further ponding at 406 and 209 MPa, based on fluid inclusions in olivines and clinopyroxenes from Terceira. Because each model has inherent uncertainties, mean values of *P–T* estimates are considered to provide the most accurate representation of thermobarometric conditions beneath Terceira, especially considering the uncertainties and the difficulty in quantifying distinct magma chambers. In our calculations, however, the more primitive clinopyroxene cores consistently yield higher pressure estimates than the mantke and rim sections of the crystals, which is geologically reasonable and internally consistent. This suggests that, although mineral-only thermobarometers may carry uncertainties related to calibration and the absence of explicit thermodynamic constraints, relative pressure differences recorded by individual crystals are robust. Consequently, our interpretation of a dynamic, multi-stage magmatic plumbing system remains valid. Pressure estimates for cores, mantles, and rims indicate at least two crystallisation environments: one producing cores and mantles at approximately 200–500 MPa, and another producing mantles and rims at around 0–250 MPa. Therefore we conclude that despite the considerable uncertainties associated with the thermobarometers used, polybaric storage is likely, as reflected in the diversity of observed crystal textures, even if the details of this cannot currently be elucidated.

5.4 Timing of pre-eruptive magmatic processes

Clinopyroxenes display a wide range of compositional and textural differences, both between eruptive centres and within individual samples. Type I and II crystals, in particular, indicate the existence of at least two compositionally distinct magmatic environments: a colder, low-Cr environment (Type I clinopyroxene; cores) and a hotter, high-Cr environment (Type II clinopyroxene). This hotter, more primitive environment also gave rise to the high-Cr recharge bands and rims present in other crystals, including the rims of Type I and Type IV clinopyroxene crystals. To gain further insight into pre-eruptive processes, we calculated pre-eruptive timescales for a representative selection of samples (Fig. 16). Calculated timescales of the last period of rim crystallisation, and thus the last period of growth prior to eruption, are, accounting for uncertainties, in the order of several months to up to 8 years (Fig. 17). The measured profile and modelled diffusion profile of a Type IV crystal are shown in Fig. 16. The average timescale from the last period of rim crystallisation is 10 months, and most of the modelled crystals yield timescales of less than 1 year. Two of the clinopyroxene crystals were modelled in two steps: from high-Cr core or recharge band to mantle, then mantle to rim. Core to rim timescales were comparable between both crystals, averaging 6.5 months, while mantle to rim timescales show greater variability. Clinopyroxenes from the same sample show diversity in timescales, e.g. from 4.1 to 22.6 months in CFZ sample T14 and from 3.8 to 33.9 months in EFZ sample T43. The range in calculated timescales suggests that ascending magma mobilised crystals from multi-level storage zones in which crystals had remained for variable lengths of time prior to eruption.

Although some olivine zoning features could be related to melt differentiation during growth, we assume that most compositional profiles are related to diffusion-driven disequilibrium between olivine and melt during crystal transport in the plumbing system. This is supported by the absence of correlated evolution between the olivine Fo-content and incompatible elements such as Al [Mutch et al. 2019]. Timescales were therefore calculated using core–rim Fe–Mg diffusion profiles. For simplicity, we focused on Type I (normal zoning) and Type III (reversed zoning) crystals. Diffusion profiles were obtained for crystals from the different eruptive centres (Fig. 16). The resulting timescales range from a few days to 5.5 years (Fig. 17). In general, the diffusion timescales obtained for olivine agree within error with those derived from clinopyroxene. The only exception is the CFZ, where long diffusive timescales were not observed in olivine (maximum ~3 months), whereas modelling of clinopyroxene profiles yielded timescales of up to ~2 years.

5.5 Plumbing system model

Based on the textural relationship observed in the main types of crystals as well as the results of thermobarometric calculations, we built a representative plumbing system for Terceira. Assuming a crustal density of 2500 $kg\,m^{-3}$ [Zanon and Pi-

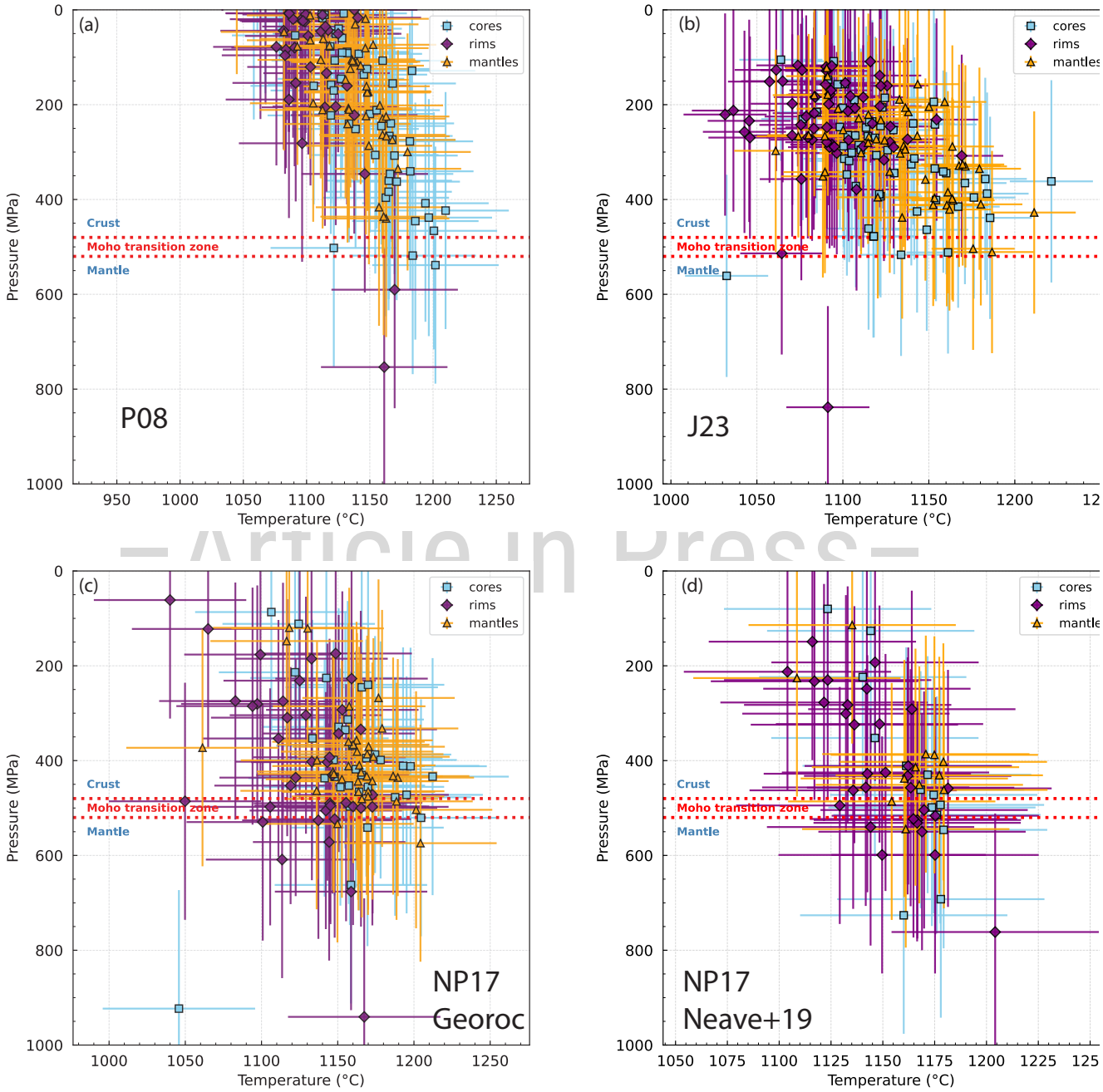

Figure 14: Results of the three thermobarometric models used to determine clinopyroxene core, mantle, and rim crystallisation pressures and temperatures: (a) results from iterating equations 32b and 32d of Putirka [2008]; (b) results from the machine-learning algorithm of Jorgenson et al. [2022]; (c) results from the model of Neave and Putirka [2017] using matched liquid compositions from Terceira's bulk rock data in Georoc; (d) results from the model of Neave and Putirka [2017] using matched liquid compositions of experimental liquids from Neave et al. [2019]. Equilibrium criteria for clinopyroxene-liquid matching are described above in the main text.

mentel 2015], thermobarometric evaluation of clinopyroxene cores, mantles and rims from Terceira in conjunction with the variety of textures observed in olivine, clinopyroxene and plagioclase indicate several storage environments. We suggest that the crust beneath Terceira hosts a deep storage zone at ~ 450 MPa and 18–20 km where Cr-rich basalts originate. We also find a mid-crustal region at around 200–250 MPa and 10 km depth where most mantle and remaining core compositions originate and resorption occurs due to repeated magma replenishment. Finally, magma ponds in a shallower zone in the upper crust at around 3 km where rims may crystallise and pre-existing evolved magma reservoirs(s) experience recharge by more primitive ascending magmas (Fig. 18). This agrees with the findings of Jeffery et al. [2017], who propose a shallow crustal storage zone at depths of around 2–4 km where evolved peralkaline trachytes and rhyolites originate, and with

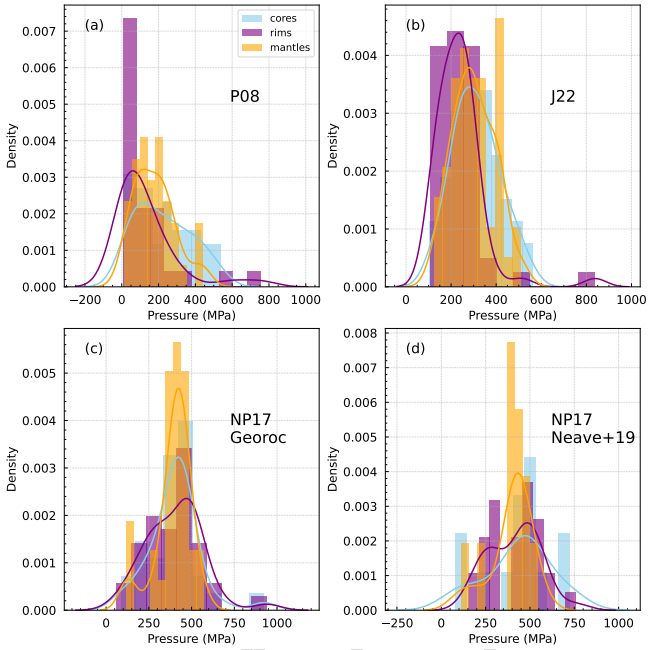

Figure 15: Summary of clinopyroxene core, rim and mantle barometric distributions obtained using the models described in Figure 14.

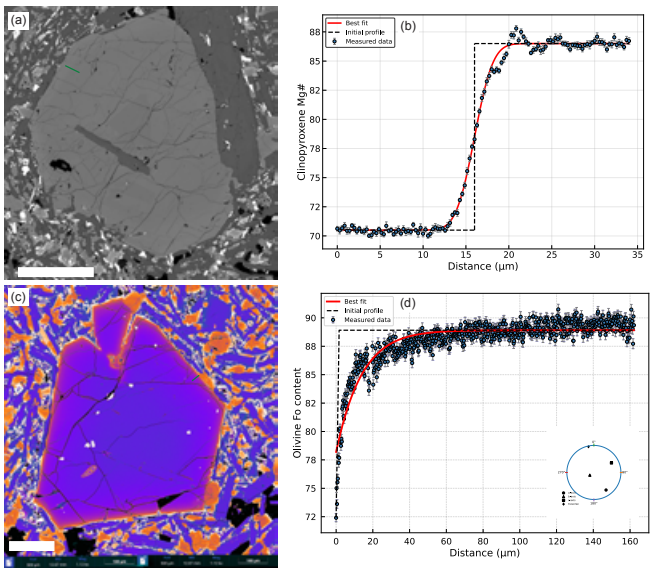

Figure 16: Examples of diffusion profiles. (a) Clinopyroxene BSE image showing distinct core and rim compositions. (b) BSE extracted clinopyroxene composition with best fit diffusion profile. The boundary conditons (initial profile) for diffusion modelling are also shown. (c) False-color olivine crystals showing compositonal zoning from core to rim. (d) BSE extracted olivine composition with best fit diffusion profile. The inset is a stereographic lower-hemisphere plot depicting the angular relation between the main crystallographic axes in olivine and the direction of the analytical traverse (cross).

the estimated depth of the deepest magma ponding zone beneath Terceira, which Zanon et al. [2023] estimate at around 17 km beneath the fissure zone and around 20 km along the northwestern axis of the fissure zone, based on microthermometric data on CO_2-rich fluid inclusions in mafic magmas.

The CFZ basalts erupted contemporaneously with short trachytic flows and domes on the eastern flank of Santa Barbara and may be viewed as off-rift basalts for this reason. The presence of evolved mush pockets beneath Terceira capable of producing trachytes has already been established [D'Oriano et al. 2017; Jeffery et al. 2017]; primitive melts ascending through the system may either bypass these evolved mush pockets and erupt at the surface as basalts (e.g. rift basalts), or interact with these reservoirs, promoting destabilisation and subsequent eruption of trachytic material. Extensional tectonics along the rift axis promote rapid magma ascent along closely spaced dykes which likely contain a large proportion of the magma within the system [Searle 1980; Trippanera et al. 2014; Pimentel et al. 2016], which will result in local heating of the crust and relatively little cooling and differentiation during magma ascent. Off-rift basalts by comparison may rise as a result of their buoyancy (e.g. Mungall and Martin [1995]) through colder, brittle crust, and thus differentiate at greater depth [Kahl et al. 2021]. Magmatism on Terceira is therefore strongly influenced by the Terceira Rift that bisects the island, and the felsic products result directly from the fractional crystallisation of both off- and on-rift basalts to produce the various felsic compositions found at Terceira [Jeffery et al. 2016; Pimentel et al. 2016; Jeffery et al. 2017].

We propose that the crustal architecture beneath Terceira consists of discrete melt pockets that are connected by dykes within a, possibly mush-bearing, magmatic system [Humphreys et al. 2025]. Primitive and evolved olivine, clinopyroxene and plagioclase macrocryst cores are formed within compositionally and thermally distinct magmatic environments, located within the lower to middle crust. Integrating major element, trace element and thermobarometric data demonstrates that melts enriched and depleted in Mg, Cr and Ni are both present at depth and give rise to different mineral textures and compositions. We conclude that primitive, Mg-, Cr- and Ni-enriched, olivine-rich melts ascend to the lower crust at around 450 MPa where they encounter the partially crystallised mush, causing stalling and slow cooling of the melt which promoted the growth of large olivine crystals. Later magma injection into this reservoir resulted in thermal erosion and entrainment of olivine crystals and subsequent growth of subhedral to euhedral clinopyroxene macrocrysts. The presence of reversely zoned olivine crystals with more evolved core compositions, Type I clinopyroxenes with Cr-poor, patchy cores and sieve textured, high-Ca Type III plagioclase cores indicate a storage region in the mid-crust, perhaps between 200–300 MPa, which is tapped by mafic recharge events that change compositions and *P*–*T* conditions within the melt pocket, give rise to disequilibrium textures within cores and mantles, and produce more primitive rim compositions. Previous mafic recharge events likely transported unzoned, Cr-rich crystals to this same mid-crustal storage region where the magma stalled and Type IV crystals became resorbed at the influx of further hot, primitive magma, producing Type II clinopyroxenes with high-Cr, high-Mg, anhedral cores. These multiple magma replenish-

Figure 17: Summary of timescales and related errors (see text) calculated from the injection of the mafic magma to eruption. (a) Timescales calculated from clinopyroxene crystals. (b) Timescales calculated from olivine crystals.

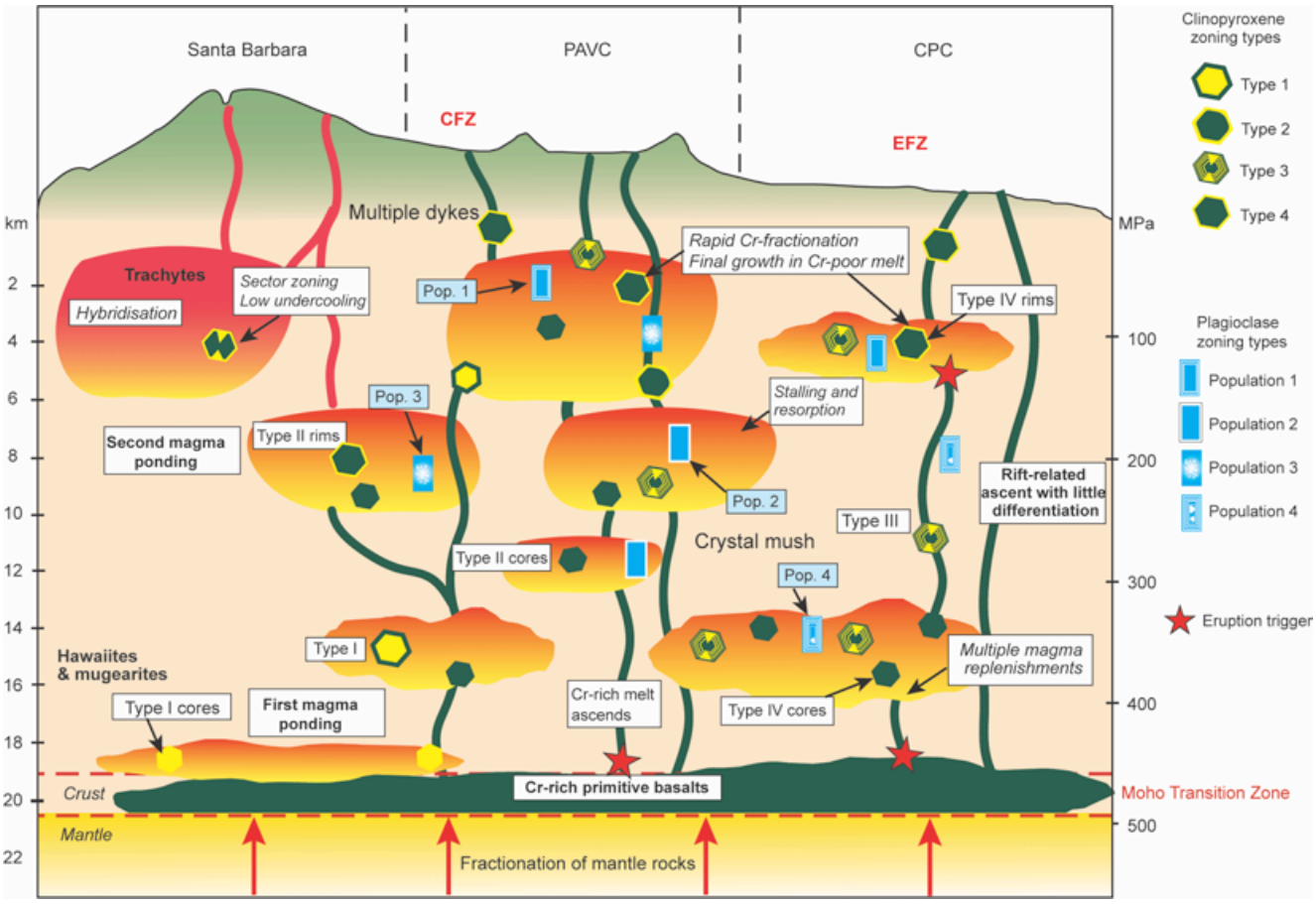

Figure 18: Schematic model of the plumbing system beneath Terceira. Mantle-derived basalts ascend and pond between 400-500 MPa, where they either ascend without differentiation (rift-related) or undergo further stages of differentiation within a multi-levels storage one connected by dykes. The origin of clinopyroxene and plagioclase zoning is also illustrated. The ascent of hot, primitive basalts promotes further differentiation and remobilisation of stalled crystals.

ments also likely produced oscillatory zoning due to changes in the intensive variables within the storage region, exemplified by Type III clinopyroxenes and Type IV plagioclase. As the melts continue to evolve in the upper crust at around 100 MPa, the melt is depleted in Cr as most of the Cr has been incorporated into growing crystals. Deep, recharging melts cannot reach these shallow storage regions, which continue to evolve and eventually become the source of trachytic and rhyolitic magmas.

The crustal architecture beneath Terceira is structurally similar to other OIB such as the Canary Islands [Stroncik et al. 2009; Klügel et al. 2015; Scarrow et al. 2024] and off-rift locations such as Snæfellsnes Peninsula in Iceland [Kahl et al. 2021] in that it is made up of a magmatic system with multiple interconnected melt pockets that promote varying levels of differentiation throughout the crust. Primitive mantle-derived basalts can either interact with mush and melt pockets in the magmatic system where they undergo differentiation, or travel straight to the surface with little differentiation. Magma in the Azores ascends from the mantle due to extensional tectonics and is thought to collect at the Moho transition zone, which acts as a filter for primitive mantle-derived magmas, promoting fractional crystallisation of ultramafic dunites, harzburgites and pyroxenites [Zanon and Pimentel 2015]. Here the magma is mobilised in response to tectonic stresses [Zanon et al. 2013; Trippanera et al. 2014; Zanon and Pimentel 2015].

6 Conclusions

In this study we present a comprehensive approach to constraining the plumbing system architecture of Terceira, in which we combine petrographical observations, whole-rock geochemistry, textural analysis of dominant phenocryst phases, thermobarometry and insights into the timescales of pre-eruptive processes. We present the first detailed insight into clinopyroxene chemistry and zoning patterns in the Azores, and demonstrate the applicability of multi-element mapping in elucidating chemical zoning in greater detail than spot analyses and BSE images can provide:

- We find cryptic Cr and Ni zoning in clinopyroxene that only becomes clear when performing elemental mapping, but offers unique insights into magmatic histories.

- Quantitative LA-ICP-TOF-MS elemental maps provide a detailed overview of trace element zoning in clinopyroxene and show that cores and rims which grew in more evolved melts are more enriched in REE; REES also show an affinity for partitioning into prism sectors over hourglass sectors.

- High-Cr and -Ni zones indicate that mafic recharge often does not trigger an eruption but instead promotes the dissolution and transport of early formed crystals.

Clinopyroxene thermobarometry and mineral zoning indicate magma storage in a vertically extensive magmatic system extending from the Moho at around 450 MPa. Variable storage depths between different volcanic edifices and lava flows, and even within samples, indicate that the reservoir comprises a multi-level stacked storage system with ephemeral melt pockets that are interconnected by dykes. Geochemically distinct primary melts differentiate to varying degrees and produce on- and off-rift melt compositions, which both crystallise an assemblage of high-An plagioclase, high-Cr and -Ni clinopyroxene and high-Fo olivine, producing basaltic melts that undergo a series of stages of differentiation. The plumbing system comprises multiple melt-rich reservoirs where crystals grow under dynamic *P–T* and compositional conditions to produce a wide variety of textures, influenced by multiple recharge events and protracted periods of stalling. Timescales of the final period of rim growth prior to eruption are on average 10 months, and the longest calculated timescales are around 3 years.

Author Contributions

KS - data acquisition, writing; ON - project design, acquisition of funding, supervision; data acquisition, writing; DAN - supervision, writing; YZ - editing; TVG - data acquisition; TVH - data acquisition; TVA - data acquisition; JBG - data acquisition; FK - editing, SK - editing; JVDA - data acquisition BC - supervision, writing.

Acknowledgements

ON acknowledges support from the FWO through an Odysseus grant. TVA acknowledges the Research Foundation Flanders for his postdoctoral research fellowship (1218423N). DAN acknowledges support from NERC (NE/T011106/1).

Data Availability

All data are provided as supplementary material in the Zenodo repository: https://zenodo.org/records/19126595.

Copyright Notice

References

Adam, C., P. Madureira, J. M. Miranda, N. Lourenço, M. Yoshida, and D. Fitzenz (2013). "Mantle dynamics and characteristics of the Azores plateau". *Earth and Planetary Science Letters* 362, pages 258–271. DOI: 10.1016/j.epsl.2012.11.018.

Ágreda-López, M., V. Parodi, A. Musu, C. Jorgenson, A. Carfì, F. Mastrogiovanni, L. Caricchi, D. Perugini, and M. Petrelli (2024). "Enhancing machine learning thermobarometry for clinopyroxene-bearing magmas". *Computers Geosciences* 193, page 105707. DOI: https://doi.org/10.1016/j.cageo.2024.105707.

Andersen, J. C. Ø. and D. H. Lindsley (1985). "New (and final!) models for the Ti–magnetite/ilmenite geothermometer and oxygen barometer". *AGU Spring Meeting Eos Transactions* 66(18), page 416. DOI: 10.1029/EO066i018p00416.

Andrews, B. J. (2022). "Plagioclase population dynamics and zoning in response to changes in temperature and pressure Figure". *American Mineralogist* 106, pages 1438–1452. DOI: 10.2138/am-2022-8130.

Anenburg, M. and M. J. Williams (2022). "Quantifying the tetrad effect, shape components, and Ce-Eu-Gd anomalies in rare earth element patterns". *Mathematical Geosciences* 54, pages 47–70. DOI: 10.1007/s11004-021-09982-3.

Annen, C., J. Blundy, and R. Sparks (2006). "The genesis of intermediate and silicic magmas in deep crustal hot zones". *Journal of Petrology* 47(3), pages 505–539. DOI: 10.1093/petrology/egi084.

Arnould, M., J. Ganne, N. Coltice, and X. Feng (2019). "Northward drift of the Azores plume in the Earth's mantle". *Nature Communications* 10, pages 1–8. DOI: 10.1038/s41467-019-08512-4.

Asimow, P. D., J. E. Dixon, and C. H. Langmuir (2004). "A hydrous melting and fractionation model for mid-ocean ridge basalts: Application to the Mid-Atlantic Ridge near the Azores". *Geochemistry, Geophysics, Geosystems* 5, pages 1–24. DOI: 10.1029/2003GC000614.

Bacon, C. R. and M. M. Hirschmann (1988). "Mg/Mn partitioning as a test for equilibrium between coexisting Fe-Ti oxides". *American Mineralogist* 73, pages 57–61. DOI: 10.2138/am-1988-73-1-57.

Beier, C., K. M. Haase, and S. P. Turner (2012). "Conditions of melting beneath the Azores". *Lithos* 144–145, pages 1–11. DOI: 10.1016/j.lithos.2012.07.001.

Beier, C., S. Turner, T. Plank, and W. White (2010). "A preliminary assessment of the symmetry of source composition and melting dynamics across the Azores plume". *Geochemistry, Geophysics, Geosystems* 11. DOI: 10.1029/2010GC003124.

Bonatti, E. (1990). "Not so hot "hot spots" in the oceanic mantle". *Science* 250, pages 107–111. DOI: 10.1126/science.250.4978.107.

Bourdon, B., S. P. Turner, and N. M. Ribe (2005). "Partial melting and upwelling rates beneath the Azores from a U-series isotope perspective". *Earth and Planetary Science Letters* 239, pages 42–56. DOI: 10.1016/j.epsl.2005.08.009.

Calvert, A. T., R. B. Moore, J. P. McGeehin, and A. M. Rodrigues da Silva (2006). "Volcanic history and 40Ar/39Ar and 14C geochronology of Terceira Island, Azores, Portu-

gal". *Journal of Volcanology and Geothermal Research* 156, pages 103–115. DOI: 10.1016/j.jvolgeores.2006.03.008.

Cannat, M. et al. (1999). "Mid-Atlantic Ridge-Azores hotspot interactions: Along-axis migration of a hotspot-derived event of enhanced magmatism 10 to 4 Ma ago". *Earth and Planetary Science Letters* 173, pages 257–269. DOI: 10.1016/S0012-821X(99)00249-8.

Caracciolo, A., M. Kahl, E. Bali, H. Gudfinnsson, S. A. Halldórsson, and M. E. Hartley (2021). "Timescales of crystal mush mobilization in the Bárðarbunga-Veiðivötn volcanic system based on olivine diffusion chronometry". *American Mineralogist* 106, pages 1083–1096. DOI: 10.2138/am-2021-7775.

Carracedo, J. C., S. Day, H. Guillou, E. Rodriguez Badiolas, J. A. Canas, and F. J. Perez Torrado (1998). "Hotspot volcanism close to a passive continental margin: the Canary Islands". *Geological Magazine* 135, pages 591–604. DOI: 10.1017/S0016756898005727.

Casas, D., A. Pimentel, J. Pacheco, E. Martorelli, A. Sposato, G. Ercilla, B. Alonso, and F. Chiocci (2018). "Serreta 1998–2001 submarine volcanic eruption, offshore Terceira (Azores): Characterization of the vent and inferences about the eruptive dynamics". *Journal of Volcanology and Geothermal Research* 356, pages 127–140. DOI: 10.1016/j.jvolgeores.2018.03.012.

Chamberlain, K. J., J. Barclay, K. J. Preece, R. J. Brown, and J. P. Davidson (2019). "Lower Crustal Heterogeneity and Fractional Crystallisation Control Evolution of Small Volume Magma Batches at Ocean Island Volcanoes (Ascension Island, South Atlantic)". *Journal of Petrology* 60, pages 1489–1522. DOI: 10.1093/petrology/egz063.

Chicchi, L., L. Bindi, D. Fanelli, and S. Tommasini (2023). "Frontiers of thermobarometry: GAIA, a novel Deep Learning-based tool for volcano plumbing systems". *Earth and Planetary Science Letters* 620, page 118352. DOI: 10.1016/j.epsl.2023.118352.

Churikova, T. G., B. V. Ivanov, J. Eichelberger, G. Wörner, B. Browne, and P. Izbekov (2013). "Major and trace element zoning in plagioclase from Kizimen Volcano (Kamchatka): Insights into magma-chamber processes". *Journal of Volcanology and Seismology* 7, pages 112–130. DOI: 10.1134/S0742046313020067.

Cooper, K. M. and A. J. R. Kent (2014). "Rapid remobilization of magmatic crystals kept in cold storage". *Nature* 506, pages 480–483. DOI: 10.1038/nature12968.

Costa, F., L. A. Coogan, and S. Chakraborty (2010). "The time scales of magma mixing and mingling involving primitive melts and melt-mush interaction at mid-ocean ridges". *Contributions to Mineralogy and Petrology* 159, pages 371–387. DOI: 10.1007/s00410-009-0453-5.

Costa, F., R. Dohmen, and S. Chakraborty (2008). "Time scales of magmatic processes from modeling the zoning patterns of crystals". *Reviews in Mineralogy and Geochemistry* 69, pages 545–594. DOI: 10.2138/rmg.2008.69.16.

Costa, F., T. Shea, and T. Ubide (2020). "Diffusion chronometry and the timescales of magmatic processes". *Nature Reviews Earth & Environment* 1, pages 201–214. DOI: 10.1038/s43017-020-0041-9.

Couperthwaite, F. K., D. J. Morgan, J. Harvey, and M. Kahl (2022). "Pre-eruptive timescales from the historical Hapaimamo eruption at Mauna Loa, Hawai'i". *Journal of Volcanology and Geothermal Research* 432, page 107690. DOI: 10.1016/j.jvolgeores.2022.107690.

D'Mello, N. G., G. F. Zellmer, G. Kereszturi, T. Ubide, J. N. Procter, and R. B. Stewart (2023). "Crystal entrainment from cool, low-silica rocks into hot, high-silica melts: diverse primary melt compositions at Taranaki volcano, New Zealand". *Journal of the Geological Society* 180(3), jgs2022–036. DOI: 10.1144/jgs2022-036.

D'Oriano, C., P. Landi, A. Pimentel, and V. Zanon (2017). "Magmatic processes revealed by anorthoclase textures and trace element modeling: The case of the Lajes Ignimbrite eruption (Terceira Island, Azores)". *Journal of Volcanology and Geothermal Research* 347, pages 44–63. DOI: 10.1016/j.jvolgeores.2017.06.008.

Dasgupta, R., M. G. Jackson, and C. T. A. Lee (2010). "Major element chemistry of ocean island basalts - Conditions of mantle melting and heterogeneity of mantle source". *Earth and Planetary Science Letters* 289, pages 377–392. DOI: 10.1016/j.epsl.2009.11.032.

Davies, G. R., A. N. Halliday, D. Lee, S. Tommasini, C. R. Paslick, J. G. Fitton, and D. E. James (1995). "Incompatible trace elements in OIB and MORB and source enrichment in the sub-oceanic mantle". *Earth and Planetary Science Letters* 133, pages 379–395. DOI: 10.1016/0012-821X(95)00095-X.

Del Fresno, C. et al. (2023). "Magmatic plumbing and dynamic evolution of the 2021 La Palma eruption". *Nature Communications* 14, pages 1–11. DOI: 10.1038/s41467-023-38669-5.

Di Stefano, F., S. Mollo, T. Ubide, C. M. Petrone, J. Caulfield, P. Scarlato, M. Nazzari, D. Andronico, and E. Del Bello (2020). "Mush cannibalism and disruption recorded by clinopyroxene phenocrysts at Stromboli volcano: New insights from recent 2003–2017 activity". *Lithos* 360, page 105440. DOI: 10.1016/j.lithos.2020.105440.

Dohmen, R., K. Faak, and J. D. Blundy (2017). "Chronometry and speedometry of magmatic processes using chemical diffusion in olivine, plagioclase and pyroxenes". *Reviews in Mineralogy and Geochemistry* 83, pages 535–575. DOI: 10.2138/rmg.2017.83.18.

Downes, M. J. (1974). "Sector and oscillatory zoning in calcic augites from M. Etna, Sicily". *Contributions to Mineralogy and Petrology* 47, pages 187–196. DOI: 10.1007/BF00384832.

Elardo, S. M. and C. K. Shearer (2014). "Magma chamber dynamics recorded by oscillatory zoning in pyroxene and olivine phenocrysts in basaltic lunar meteorite Northwest Africa 032". *American Mineralogist* 99(2-3), pages 355–368. DOI: 10.2138/am.2014.4538.

Fitton, J. G. (2007). "The OIB paradox". *Special Paper of the Geological Society of America* 430, pages 387–412. DOI: 10.1130/2007.2430(18).

Foley, S. F., D. Prelevic, T. Rehfeldt, and D. E. Jacob (2013). "Minor and trace elements in olivines as probes into early igneous and mantle melting processes". *Earth and Planetary Science Letters* 363, pages 181–191. DOI: 10.1016/j.epsl.2012.12.013.

Gaspar, J. L., G. Queiroz, J. M. Pacheco, T. Ferreira, N. Wallenstein, M. H. Almeida, and R. Coutinho (2003). "Basaltic lava balloons produced during the 1998-2001 Serreta submarine ridge eruption (Azores)". *Geophysical Monograph Series* 140, pages 205–212. DOI: 10.1029/140GM15.

Gertisser, R. et al. (2010). "Ignimbrite stratigraphy and chronology on Terceira Island, Azores". *Special Paper of the Geological Society of America* 464, pages 133–154. DOI: 10.1130/2010.2464(07).

Ginibre, C., G. Wörner, and A. Kronz (2007). "Crystal zoning as an archive for magma evolution". *Elements* 3, pages 261–266. DOI: 10.2113/gselements.3.4.261.

Ginibre, C., G. Wörner, and A. Kronz (2002). "Minor- and trace-element zoning in plagioclase: implications for magma chamber processes at Parinacota volcano, northern Chile". *Contributions to Mineralogy and Petrology* 143(3), pages 300–315. DOI: 10.1007/s00410-002-0392-x.

Gleeson, M. L., S. A. Gibson, and M. J. Stock (2020). "Upper mantle mush zones beneath low melt flux ocean island volcanoes: insights from Isla Floreana, Galápagos". *Journal of Petrology* 61(11-12), egaa094.

Hattori, K. and H. Sato (1996). "Magma evolution recorded in plagioclase zoning in 1991 Pinatubo eruption products". *American Mineralogist* 81, pages 982–994. DOI: 10.2138/am-1996-9-1007.

Hildenbrand, A., D. Weis, P. Madureira, and F. O. Marques (2014). "Recent plate re-organization at the Azores Triple Junction: Evidence from combined geochemical and geochronological data on Faial, S. Jorge and Terceira volcanic islands". *Lithos* 210–211, pages 27–39. DOI: 10.1016/j.lithos.2014.07.016.

Hofmann, A. W. (2003). *Sampling Mantle Heterogeneity through Oceanic Basalts: Isotopes and Trace Elements*. Treatise on Geochemistry. Amsterdam: Elsevier. DOI: 10.1016/B0-08-043751-6/03016-9.

Humphreys, E. R. and Y. Niu (2009). "On the composition of ocean island basalts (OIB): The effects of lithospheric thickness variation and mantle metasomatism". *Lithos* 112, pages 118–136. DOI: 10.1016/j.lithos.2009.03.002.

Humphreys, M. C. S., J. D. Blundy, and R. S. J. Sparks (2006). "Magma evolution and open-system processes at Shiveluch Volcano: Insights from phenocryst zoning". *Journal of Petrology* 47, pages 2303–2334. DOI: 10.1093/petrology/egl049.

Humphreys, M., O. Namur, W. A. Bohrson, P. Bouilhol, G. F. Cooper, K. M. Cooper, C. Huber, C. J. Lissenberg, E. Morgado, and F. J. Spera (2025). "Crystal mush processes and crustal magmatism". *Nature Reviews Earth & Environment*, pages 1–16. DOI: 10.1038/s43017-024-00365-1.

Jarosewich, E., J. A. Nelen, and J. A. Norberg (1980). "Reference samples for electron microprobe analysis". *Geostandards and Geoanalytical Research* 4, pages 43–47. DOI: 10.1111/j.1751-908X.1980.tb00532.x.

Jarosewich, E. (2002). "Smithsonian microbeam standards". *Journal of Research of the National Institute of Standards and Technology* 107(6), page 681. DOI: 10.6028/jres.107.064.

Jeffery, A. J., R. Gertisser, B. O'Driscoll, J. M. Pacheco, S. Whitley, A. Pimentel, and S. Self (2016). "Temporal evolution of a post-caldera, mildly peralkaline magmatic system: Furnas volcano, São Miguel, Azores". *Contributions to Mineralogy and Petrology* 171, page 42. DOI: 10.1007/s00410-016-1266-7.

Jeffery, A. J., R. Gertisser, S. Self, A. Pimentel, B. O'Driscoll, and J. M. Pacheco (2017). "Petrogenesis of the peralkaline ignimbrites of Terceira, Azores". *Journal of Petrology* 58, pages 2365–2402. DOI: 10.1093/petrology/egx070.

Jochum, K. P. et al. (2006). "MPI-DING reference glasses for in situ microanalysis: New reference values for element concentrations and isotope ratios". *Geochemistry, Geophysics, Geosystems* 7. DOI: 10.1029/2006GC001300.

– (2011). "Determination of reference values for NIST SRM 610-617 glasses following ISO guidelines". *Geostandards and Geoanalytical Research* 35, pages 397–429. DOI: 10.1111/j.1751-908X.2011.00120.x.

Jochum, K. P., M. Willbold, I. Raczek, B. Stoll, and K. Herwig (2005). "Chemical characterisation of the USGS reference glasses GSA-1G, GSC-1G, GSD-1G, GSE-1G, BCR-2G, BHVO-2G and BIR-1G using EPMA, ID-TIMS, ID-ICP-MS and LA-ICP-MS". *Geostandards and Geoanalytical Research* 29, pages 285–302. DOI: 10.1111/j.1751-908X.2005.tb00964.x.

Jorgenson, C., O. Higgins, M. Petrelli, F. Bégué, and L. Caricchi (2022). "A machine learning-based approach to clinopyroxene thermobarometry: Model optimization and distribution for use in Earth Sciences". *Journal of Geophysical Research: Solid Earth* 127, pages 1–21. DOI: 10.1029/2021JB022490.

Jorgenson, C., L. Caricchi, M. Chiaradia, M. Ágreda-López, and G. Giordano (2024). "Rapid accumulation and ascent precedes caldera forming eruption of low viscosity magma". *Contributions to Mineralogy and Petrology* 179(2), page 16.

Kahl, M., E. Bali, G. H. Guðfinnsson, D. A. Neave, T. Ubide, Q. H. A. Van Der Meer, and S. Matthews (2021). "Conditions and dynamics of magma storage in the Snæfellsnes volcanic zone, western Iceland: Insights from the Búðahraun and Berserkjahraun eruptions". *Journal of Petrology* 62, pages 1–29.

Kahl, M., S. Chakraborty, F. Costa, and M. Pompilio (2011). "Dynamic plumbing system beneath volcanoes revealed by kinetic modeling, and the connection to monitoring data: An example from Mt. Etna". *Earth and Planetary Science Letters* 308, pages 11–22.

Kahl, M., S. Chakraborty, M. Pompilio, and F. Costa (2015). "Constraints on the nature and evolution of the magma plumbing system of Mt. Etna volcano (1991-2008) from a combined thermodynamic and kinetic modelling of the compositional record of minerals". *Journal of Petrology* 56, pages 2025–2068.

Kahl, M., M. Viccaro, T. Ubide, D. J. Morgan, and D. B. Dingwell (2017). "A branched magma feeder system during the

1669 eruption of Mt Etna: Evidence from a time-integrated study of zoned olivine phenocryst populations". *Journal of Petrology* 58, pages 443–472.

Kelsey, C. H. (1965). "Calculation of the CIPW Norm". *Mineralogical Magazine* 34, pages 276–282.

Kirkpatrick, R. J., L.-C. Kuo, and J. Melchior (1981). "Crystal growth in incongruently-melting compositions: programmed cooling experiments with diopside". *American mineralogist* 66(3-4), pages 223–241.

Klügel, A., M.-A. Longpré, L. García-Cañada, and J. Stix (2015). "Deep intrusions, lateral magma transport and related uplift at ocean island volcanoes". *Earth and Planetary Science Letters* 431, pages 140–149.

Kouchi, A., Y. Sugawara, K. Kashima, and I. Sunagawa (1983). "Laboratory growth of sector zoned clinopyroxenes in the system $CaMgSi_2O_6 - CaTiAl_2O6$". *Contributions to Mineralogy and Petrology* 83, pages 177–184.

Le Maitre, R. W. et al. (2002). *Igneous Rocks. A classification and glossary of terms*. 2nd edition. Cambridge University Press.

Leung, I. S. (1974). "Sector-zoned titanaugites: morphology, crystal chemistry, and growth". *American Mineralogist* 59, pages 127–138. DOI: 10.2138/am-1974-59-127.

Li, W.-R., O. Shorttle, J. Maclennan, S. Matthews, Y. Zhang, O. Namur, C. R. Soderman, and D. Geist (2025). "Taking the temperature of ocean islands: a petrological approach". *Journal of Petrology*, egaf033. DOI: 10.1093/petrology/egaf033.

Machado, F. (1959). "Submarine pits of the Azores plateau". *Bulletin Volcanologique* TXXI.

Maclennan, J., D. McKenzie, and K. Gronvold (2001). "Plume-driven upwelling under Central Iceland". *Earth and Planetary Science Letters* 194, pages 67–82. DOI: 10.1016/S0012-821X(01)00536-2.

Madeira, J. (2005). *The Volcanoes of Azores Islands: a world-class heritage. Examples from Terceira, Pico, and Faial Islands*. Field Trip Guide Book. IV International Symposium ProGEO on the Conservation of the Geological Heritage, page 104.

Madureira, P. et al. (2017). "The 1998–2001 submarine lava balloon eruption at the Serreta ridge (Azores archipelago): Constraints from volcanic facies architecture, isotope geochemistry and magnetic data". *Journal of Volcanology and Geothermal Research* 329, pages 13–29. DOI: 10.1016/j.jvolgeores.2016.10.009.

Madureira, P., M. Moreira, J. Mata, and C. J. Allègre (2005). "Primitive neon isotopes in Terceira Island (Azores archipelago)". *Earth and Planetary Science Letters* 233, pages 429–440. DOI: 10.1016/j.epsl.2005.02.025.

Madureira, P., M. Moreira, J. Mata, J. C. Nunes, C. Gautheron, N. Lourenço, R. Carvalho, and M. P. de Abreu (2014). "Helium isotope systematics in the vicinity of the Azores triple junction: Constraints on the Azores geodynamics". *Chemical Geology* 372, pages 62–71. DOI: 10.1016/j.chemgeo.2014.02.007.

Madureira, P., J. Mata, N. Mattielli, G. Queiroz, and P. Silva (2011). "Mantle source heterogeneity, magma generation and magmatic evolution at Terceira Island (Azores archipelago): constraints from elemental and isotopic (Sr, Nd, Hf, and Pb) data". *Lithos* 126(3-4), pages 402–418. DOI: 10.1016/j.lithos.2011.06.011.

McKenzie, D. and M. J. Bickle (1988). "The volume and composition of melt generated by extension of the lithosphere". *Journal of Petrology* 29, pages 625–679. DOI: 10.1093/petrology/29.3.625.

McKenzie, D. and R. K. O'Nions (1995). "The source region of ocean island basalts". *Journal of Petrology* 36, pages 133–159. DOI: 10.1093/petrology/36.1.133.

Métrich, N., V. Zanon, L. Créon, A. Hildenbrand, M. Moreira, and F. O. Marques (2014). "Is the 'Azores hotspot'a wetspot? Insights from the geochemistry of fluid and melt inclusions in olivine of Pico basalts". *Journal of Petrology* 55(2), pages 377–393. DOI: 10.1093/petrology/egt070.

Mollo, S., J. Blundy, P. Scarlato, S. P. De Cristofaro, V. Tecchiato, F. Di Stefano, F. Vetere, F. Holtz, and O. Bachmann (2018). "An integrated P-T-H 2 O-lattice strain model to quantify the role of clinopyroxene fractionation on REE+Y and HFSE patterns of mafic alkaline magmas: Application to eruptions at Mt. Etna". *Earth-Science Reviews* 185, pages 32–56. DOI: 10.1016/j.earscirev.2018.05.012.

Mollo, S. and J. E. Hammer (2017). "Dynamic crystallization in magmas". *European Mineralogical Union Notes in Mineralogy*, pages 373–418.

Mollo, S. and M. Masotta (2014). "Optimizing pre-eruptive temperature estimates in thermally and chemically zoned magma chambers". *Chemical Geology* 368, pages 97–103. DOI: 10.1016/j.chemgeo.2013.11.015.

Mollo, S., K. Putirka, V. Misiti, M. Soligo, and P. Scarlato (2013). "A new test for equilibrium based on clinopyroxene–melt pairs: clues on the solidification temperatures of Etnean alkaline melts at post-eruptive conditions". *Chemical Geology* 352, pages 92–100. DOI: 10.1016/j.chemgeo.2013.05.024.

Moreira, M., R. Doucelance, M. D. Kurz, B. Dupré, and C. J. Allègre (1999). "Helium and lead isotope geochemistry of the Azores archipelago". *Earth and Planetary Science Letters* 169, pages 189–205. DOI: 10.1016/S0012-821X(99)00071-1.

Moussallam, Y., M.-A. Longpré, C. McCammon, A. Gomez-Ulla, E. F. Rose-Koga, B. Scaillet, N. Peters, E. Gennaro, R. Paris, and C. Oppenheimer (2019). "Mantle plumes are oxidised". *Earth and Planetary Science Letters* 527, page 115798. DOI: 10.1016/j.epsl.2019.115798.

Müller, T., R. Dohmen, H. W. Becker, J. H. ter Heege, and S. Chakraborty (2013). "Fe-Mg interdiffusion rates in clinopyroxene: Experimental data and implications for Fe-Mg exchange geothermometers". *Contributions to Mineralogy and Petrology* 166, pages 1563–1576. DOI: 10.1007/s00410-013-0899-x.

Mungall, J. E. and R. F. Martin (1995). "Petrogenesis of basalt-comendite and basalt-pantellerite suites, Terceira, Azores, and some implications for the origin of ocean-island rhyolites". *Contributions to Mineralogy and Petrology* 119, pages 43–55. DOI: 10.1007/BF00307261.

Mutch, E. J., J. Maclennan, O. Shorttle, M. Edmonds, and J. F. Rudge (2019). "Rapid transcrustal magma movement under Iceland". *Nature Geoscience* 12(7), pages 569–574.

Nakamura, Y. (1973). "Origin of sector-zoning of igneous clinopyroxenes". *American Mineralogist: Journal of Earth and Planetary Materials* 58(11-12), pages 986–990. DOI: 10.2138/am-1973-11-1211.

Namur, O. and M. C. S. Humphreys (2018). "Trace element constraints on the differentiation and crystal mush solidification in the Skaergaard intrusion, Greenland". *Journal of Petrology* 59, pages 387–418. DOI: 10.1093/petrology/egy015.

Namur, O., M. C. Humphreys, and M. B. Holness (2014). "Crystallization of interstitial liquid and latent heat buffering in solidifying gabbros: Skaergaard intrusion, Greenland". *Journal of Petrology* 55(7), pages 1389–1427. DOI: 10.1093/petrology/egu028.

Namur, O., S. Montalbano, O. Bolle, and J. Vander Auwera (2020). "Petrology of the April 2015 eruption of Calbuco volcano, southern Chile". *Journal of Petrology* 61(8), egaa084. DOI: 10.1093/petrology/egaa084.

Nardini, N., F. Casetta, C. M. Petrone, Y. Buret, T. Ntaflos, and M. Coltorti (2024). "Modelling ancient magma plumbing systems through clinopyroxene populations: a case study from Middle Triassic volcanics (Dolomites, Italy)". *Contributions to Mineralogy and Petrology* 179, page 22. DOI: 10.1007/s00410-024-02167-4.

Neave, D. A. and K. D. Putirka (2017). "A new clinopyroxene-liquid barometer, and implications for magma storage pressures under Icelandic rift zones". *American Mineralogist* 102, pages 777–794. DOI: 10.2138/am-2017-5867.

Neave, D. A., E. Bali, G. H. Guðfinnsson, S. A. Halldórsson, M. Kahl, A.-S. Schmidt, and F. Holtz (2019). "Clinopyroxene–liquid equilibria and geothermobarometry in natural and experimental tholeiites: the 2014–2015 Holuhraun eruption, Iceland". *Journal of Petrology* 60(8), pages 1653–1680. DOI: 10.1093/petrology/egz054.

Neave, D. A. and J. Maclennan (2020). "Clinopyroxene dissolution records rapid magma ascent". *Frontiers in Earth Science* 8, page 188. DOI: 10.3389/feart.2020.00188.

Neave, D. A., A. G. Stewart, M. E. Hartley, and O. Namur (2024). "Iron valence systematics in clinopyroxene crystals from ocean island basalts". *Contributions to Mineralogy and Petrology* 179(6), page 67. DOI: 10.1007/s00410-024-02168-3.

Niu, Y., M. Wilson, E. R. Humphreys, and M. J. O'Hara (2011). "The origin of intra-plate ocean island basalts (OIB): The lid effect and its geodynamic implications". *Journal of Petrology* 52, pages 1443–1468. DOI: 10.1093/petrology/egr023.

Nunes, J. C., A. Calvert, S. Medeiros, E. A. Lima, F. Pereira, M. P. Costa, P. Barcelos, and M. R. Carvalho (2014). "Geological mapping of the central area of Terceira Island (Azores, Portugal): Associated volcanostratigraphy, ages and genetic implications on the Malha-Balcões-Chamusca lava caves system". *Comunicacoes Geologicas* 101, pages 10–13.

O'Neill, H. S. C. (2016). "The smoothness and shapes of chondrite-normalized rare earth element patterns in basalts". *Journal of Petrology* 57, pages 1463–1508. DOI: 10.1093/petrology/egw034.

Palummo, F., S. Mollo, C. Maria, B. S. Ellis, G. D. Astis, M. Nazzari, P. Scarlato, and O. Bachmann (2021). "Decoding multiple zoning patterns in clinopyroxene phenocrysts at Vulcano Island: A record of dynamic crystallization through interconnected reservoirs". *Lithos* 406–407, page 106517. DOI: 10.1016/j.lithos.2021.106517.

Paton, C., J. Hellstrom, B. Paul, J. Woodhead, and J. Hergt (2011). "Iolite: Freeware for the visualisation and processing of mass spectrometric data". *Journal of Analytical Atomic Spectrometry* 26, pages 2508–2518. DOI: 10.1039/c1ja10172b.

Perugini, D., G. Poli, and L. Valentini (2005). "Strange attractors in plagioclase oscillatory zoning: Petrological implications". *Contributions to Mineralogy and Petrology* 149, pages 482–497. DOI: 10.1007/s00410-005-0017-9.

Petrone, C. M., G. Bugatti, E. Braschi, and S. Tommasini (2016). "Pre-eruptive magmatic processes re-timed using a non-isothermal approach to magma chamber dynamics". *Nature Communications* 7, pages 1–11. DOI: 10.1038/ncomms12585.

Petrone, C. M. and et al. (2022). "Magma recharge and mush rejuvenation drive paroxysmal activity at Stromboli volcano". *Nature Communications* 13, pages 1–17. DOI: 10.1038/s41467-022-28098-2.

Pimentel, A. (2015). "Pyroclastic density current-forming eruptions on Faial and Terceira islands, Azores". PhD thesis. University of the Azores, page 232.

Pimentel, A., S. Self, J. M. Pacheco, A. J. Jeffery, and R. Gertisser (2021). "Eruption style, emplacement dynamics and geometry of peralkaline ignimbrites: Insights from the Lajes-Angra ignimbrite formation, Terceira island, Azores". *Frontiers in Earth Science* 9, pages 1–23. DOI: 10.3389/feart.2021.660175.

Pimentel, A., V. Zanon, L. V. de Groot, A. Hipólito, A. Di Chiara, and S. Self (2016). "Stress-induced comenditic trachyte effusion triggered by trachybasalt intrusion: Multidisciplinary study of the AD 1761 eruption at Terceira Island (Azores)". *Bulletin of Volcanology* 78. DOI: 10.1007/s00445-016-1037-6.

Putirka, K. D. (2008). "Thermometers and barometers for volcanic systems". *Reviews in Mineralogy and Geochemistry* 69, pages 61–120. DOI: 10.2138/rmg.2008.69.3.

Putirka, K. (1999). "Clinopyroxene+ liquid equilibria to 100 kbar and 2450 K". *Contributions to Mineralogy and Petrology* 135(2), pages 151–163.

– (2016). "Special Collection: Olivine: Rates and styles of planetary cooling on Earth, Moon, Mars, and Vesta, using new models for oxygen fugacity, ferric-ferrous ratios, olivine-liquid Fe-Mg exchange, and mantle potential temperature". *American Mineralogist* 101(4), pages 819–840. DOI: 10.2138/am-2016-5669.

Putirka, K., M. Johnson, R. Kinzler, J. Longhi, and D. Walker (1996). "Thermobarometry of mafic igneous rocks based on clinopyroxene-liquid equilibria, 0–30 kbar". *Contributions to Mineralogy and Petrology* 123, pages 92–108. DOI: 10.1007/s004100050141.

Ribe, N. M. and U. R. Christensen (1999). "The dynamical origin of Hawaiian volcanism". *Earth and Planetary Science Letters* 171, pages 517–531. DOI: 10.1016/S0012-821X(99)00190-6.

Riel, N., B. J. Kaus, E. Green, and N. Berlie (2022). "MAGEMin, an efficient Gibbs energy minimizer: application to igneous systems". *Geochemistry, Geophysics, Geosystems* 23(7), e2022GC010427.

Roeder, P. L. and R. F. Emslie (1970). "Olivine-liquid equilibrium". *Contributions to Mineralogy and Petrology* 29(4), pages 275–289. DOI: 10.1007/BF00371270.

Sauerzapf, U., D. Lattard, M. Burchard, and R. Engelmann (2008). "The titanomagnetite-ilmenite equilibrium: new experimental data and thermo-oxybarometric application to the crystallization of basic to intermediate rocks". *Journal of Petrology* 49, pages 1161–1185. DOI: 10.1093/petrology/egn034.

Scarrow, J. H., M. J. Pankhurst, O. A. Barbee, K. J. Chamberlain, D. J. Morgan, M.-A. Longpré, S. Tramontano, J. Hickey, D. A. Neave, G. K. Rollinson, A. G. Stewart, P. E. Wieser, B. C. Coldwell, W. Hernández, L. D'Auria, and N. M. Pérez (2024). "Decoding links between magmatic processes and eruption dynamics: whole-rock time series petrology of the 2021 Tajogaite eruption, La Palma". *Volcanica* 7(2), pages 953–980. DOI: 10.30909/vol.07.02.953980.

Schilling, J. G. (1975). "Azores mantle blob: Rare-earth evidence". *Earth and Planetary Science Letters* 25, pages 103–115. DOI: 10.1016/0012-821X(75)90079-1.

– (1985). "Upper mantle heterogeneities and dynamics". *Nature* 314, pages 62–65. DOI: 10.1038/314062a0.

Schoneveld, L., S. J. Barnes, H. V. Makkonen, M. Le Vaillant, D. J. Paterson, V. Taranovic, K. Y. Wang, and Y. J. Mao (2020). "Zoned pyroxenes as prospectivity indicators for magmatic Ni-Cu sulfide mineralization". *Frontiers in Earth Science* 8. DOI: 10.3389/feart.2020.00155.

Searle, R. (1980). "Tectonic pattern of the Azores spreading centre and triple junction". *Earth and Planetary Science Letters* 51, pages 415–434. DOI: 10.1016/0012-821X(80)90152-0.

Self, S. (1976). "The recent volcanology of Terceira, Azores". *Journal of the Geological Society* 132, pages 645–666. DOI: 10.1144/gsjgs.132.6.0645.

Self, S. and B. M. Gunn (1976). "Petrology, volume and age relations of alkaline and saturated peralkaline volcanics from Terceira, Azores". *Contributions to Mineralogy and Petrology* 54, pages 293–313. DOI: 10.1007/BF00380556.

Shepherd, K., O. Namur, M. J. Toplis, J. L. Devidal, and B. Charlier (2022). "Trace element partitioning between clinopyroxene, magnetite, ilmenite and ferrobasaltic to dacitic magmas: an experimental study on the role of oxygen fugacity and melt composition". *Contributions to Mineralogy and Petrology* 177, pages 1–21. DOI: 10.1007/s00410-022-01915-0.

Shore, M. and A. D. Fowler (1996). "Oscillatory zoning in minerals; a common phenomenon". *The Canadian Mineralogist* 34(6), pages 1111–1126. DOI: 10.3749/canmin.34.6.1111.

Shorttle, O., J. MacLennan, and S. M. Jones (2010). "Control of the symmetry of plume-ridge interaction by spreading ridge geometry". *Geochemistry, Geophysics, Geosystems* 11, pages 1–27. DOI: 10.1029/2010GC003088.

Stock, M. J., M. Bagnardi, D. A. Neave, J. Maclennan, B. Bernard, I. Buisman, M. L. Gleeson, and D. Geist (2018). "Integrated petrological and geophysical constraints on magma system architecture in the western Galápagos Archipelago: insights from Wolf volcano". *Geochemistry, Geophysics, Geosystems* 19(12), pages 4722–4743.

Streck, M. J. (2008). "Mineral textures and zoning as evidence for open system processes". *Reviews in Mineralogy and Geochemistry* 69(1), pages 595–622. DOI: 10.2138/rmg.2008.69.20.

Stroncik, N. A., A. Klügel, and T. H. Hansteen (2009). "The magmatic plumbing system beneath El Hierro (Canary Islands): Constraints from phenocrysts and naturally quenched basaltic glasses in submarine rocks". *Contributions to Mineralogy and Petrology* 157, pages 593–607. DOI: 10.1007/s00410-008-0356-0.

Sun, S.-S. and W. F. McDonough (1989). "Chemical and isotopic systematics of oceanic basalts: implications for mantle composition and processes". *Geological Society, London, Special Publications* 42(1), pages 313–345. DOI: 10.1144/GSL.SP.1989.042.01.24.

Tapu, A. T., T. Ubide, and M. Vasconcelos (2022). "Plumbing System Architecture of Late-Stage Hotspot Volcanoes in Eastern Australia". *Journal of Petrology* 63, pages 1–24. DOI: 10.1093/petrology/egac033.

Tepley, F. J. and J. P. Davidson (2003). "Mineral-scale Sr-isotope constraints on magma evolution and chamber dynamics in the Rum layered intrusion, Scotland". *Contributions to Mineralogy and Petrology* 145, pages 628–641. DOI: 10.1007/s00410-003-0463-0.

Trippanera, D., M. Porreca, J. Ruch, A. Pimentel, V. Acocella, J. Pacheco, and M. Salvatore (2014). "Relationships between tectonics and magmatism in a transtensive/transform setting: An example from Faial Island (Azores, Portugal)". *Bulletin of the Geological Society of America* 126, pages 164–181. DOI: 10.1130/B30813.1.

Turner, S., J. Foden, R. George, P. Evans, R. Varne, M. Elburg, and G. Jenner (2003). "Rates and processes of potassic magma evolution beneath Sangeang Api volcano, East Sunda arc, Indonesia". *Journal of Petrology* 44(3), pages 491–515. DOI: 10.1093/petrology/44.3.491.

Ubide, T., J. Caulfield, C. Brandt, Y. Bussweiler, S. Mollo, F. Di Stefano, M. Nazzari, and P. Scarlato (2019a). "Deep magma storage revealed by multi-method elemental mapping of clinopyroxene megacrysts at Stromboli volcano". *Frontiers in Earth Science* 7. DOI: 10.3389/feart.2019.00150.

Ubide, T., P. Larrea, L. Becerril, and C. Galé (2021). "Volcanic plumbing filters on ocean-island basalt geochemistry". *Geology* 50, pages 26–31. DOI: 10.1130/G49190.1.

Ubide, T., C. A. McKenna, D. M. Chew, and B. S. Kamber (2015). "High-resolution LA-ICP-MS trace element mapping of igneous minerals: In search of magma histories". *Chemical Geology* 409, pages 157–168. DOI: 10.1016/j.chemgeo.2015.05.004.

Ubide, T., S. Mollo, J.-x. Zhao, M. Nazzari, and P. Scarlato (2019b). "Sector-zoned clinopyroxene as a recorder of magma history, eruption triggers, and ascent rates". *Geochimica et Cosmochimica Acta* 251, pages 265–283. DOI: 10.1016/j.gca.2019.02.024.

Ubide, T. and B. S. Kamber (2018). "Volcanic crystals as time capsules of eruption history". *Nature Communications* 9(1), page 326. DOI: 10.1038/s41467-017-02564-1.

Ubide, T., Á. Márquez, E. Ancochea, M. J. Huertas, R. Herrera, J. J. Coello-Bravo, D. Sanz-Mangas, J. Mulder, A. MacDonald, and I. Galindo (2023). "Discrete magma injections drive the 2021 La Palma eruption". *Science Advances* 9(27), eadg4813.

Van Gerve, T. D., D. A. Neave, R. R. Almeev, F. Holtz, and O. Namur (2020). "Zoned crystal records of transcrustal magma transport, storage and differentiation: Insights from the Shatsky Rise oceanic plateau". *Journal of Petrology* 61, egaa080. DOI: 10.1093/petrology/egaa080.

Van Malderen, S. J. M., J. T. Van Elteren, and F. Vanhaecke (2015). "Development of a fast laser ablation–inductively coupled plasma–mass spectrometry cell for sub-m scanning of layered materials". *Journal of Analytical Atomic Spectrometry* 30, pages 119–125. DOI: 10.1039/C4JA00395C.

Van Orman, J. A., T. L. Grove, and N. Shimizu (2001). "Rare earth element diffusion in diopside: Influence of temperature, pressure, and ionic radius, and an elastic model for diffusion in silicates". *Contributions to Mineralogy and Petrology* 141, pages 687–703. DOI: 10.1007/s004100100233.

Vander Auwera, J., O. Namur, A. Dutrieux, C. M. Wilkinson, M. Ganerød, V. Coumont, and O. Bolle (2019). "Mantle melting and magmatic processes under La Picada Stratovolcano (CSVZ, Chile)". *Journal of Petrology* 60, pages 907–944. DOI: 10.1093/petrology/egy040.

Van Gerve, T. D., D. A. Neave, P. Wieser, H. Lamadrid, N. Hulsbosch, and O. Namur (2024). "The Origin and Differentiation of CO_2-Rich Primary Melts in Ocean Island Volcanoes: Integrating 3D X-Ray Tomography with Chemical Microanalysis of Olivine-Hosted Melt Inclusions from Pico (Azores)". *Journal of Petrology* 65(2), egae006. DOI: 10.1093/petrology/egae006.

Vogt, P. R. and W. Y. Jung (2004). "The Terceira Rift as hyper-slow, hotspot-dominated oblique spreading axis: A comparison with other slow-spreading plate boundaries". *Earth and Planetary Science Letters* 218, pages 77–90. DOI: 10.1016/S0012-821X(03)00798-7.

Wass, S. Y. (1973). "The origin and petrogenetic significance of hour-glass zoning in titaniferous clinopyroxenes". *Mineralogical Magazine* 39, pages 133–144. DOI: 10.1180/minmag.1973.039.302.01.

Watson, E. B. and Y. Liang (1995). "A simple model for sector zoning in slowly grown crystals: Implications for growth rate and lattice diffusion, with emphasis on accessory minerals in crustal rocks". *American Mineralogist* 80(11-12), pages 1179–1187. DOI: 10.2138/am-1995-11-1204.

Welsch, B., J. Hammer, A. Baronnet, S. Jacob, E. Hellebrand, and J. Sinton (2016). "Clinopyroxene in postshield Haleakala ankaramite: 2. Texture, compositional zoning and supersaturation in the magma". *Contributions to Mineralogy and Petrology* 171, pages 1–19. DOI: 10.1007/s00410-016-1274-7.

White, W. M., M. D. M. Tapia, and J.-G. Schilling (1979). "The petrology and geochemistry of the Azores islands". *Contributions to Mineralogy and Petrology* 69, pages 201–213. DOI: 10.1007/BF00379886.

Wieser, P. E., J. R. K. Adam, and C. B. Till (2023). "Barometers Behaving Badly II: A Critical Evaluation of Cpx-Only and Cpx-Liq Thermobarometry in Variably-Hydrous Arc Magmas". *Journal of Petrology* 64, egad050. DOI: 10.1093/petrology/egad050.

Wieser, P. E., M. Petrelli, J. Lubbers, E. Wieser, S. Özaydın, A. J. R. Kent, and C. B. Till (2022). "Thermobar: An open-source Python3 tool for thermobarometry and hygrometry". *Volcanica* 5, pages 349–384. DOI: 10.30909/vol.05.03.349384.

Wilson, T. J. (1963). "A possible origin of the Hawaiian Islands". *Canadian Journal of Physics* 41, pages 863–870. DOI: 10.1139/p63-112.

Winpenny, B. and J. Maclennan (2011). "A partial record of mixing of mantle melts preserved in Icelandic phenocrysts". *Journal of Petrology* 52(9), pages 1791–1812.

Zanon, V., U. Kueppers, J. M. Pacheco, and I. Cruz (2013). "Volcanism from fissure zones and the Caldeira central volcano of Faial Island, Azores archipelago: Geochemical processes in multiple feeding systems". *Geological Magazine* 150, pages 536–555. DOI: 10.1017/S0016756812000725.

Zanon, V. and A. Pimentel (2015). "Spatio-temporal constraints on magma storage and ascent conditions in a transtensional tectonic setting: The case of the Terceira Island (Azores)". *American Mineralogist* 100, pages 795–805. DOI: 10.2138/am-2015-5110.

Zanon, V., R. Silva, and C. Goulart (2023). "The crust-mantle transition beneath the Azores region (central-north Atlantic Ocean)". *Contributions to Mineralogy and Petrology* 178, pages 1–17. DOI: 10.1007/s00410-023-02088-2.

Zanon, V., N. Métrich, and C. D'Oriano (2024). "Geochemical processes in the roots of the Azores magmatic systems". *Contributions to Mineralogy and Petrology* 179(6), page 64. DOI: 10.1007/s00410-024-02179-1.

Zellmer, G. F. (2021). "Gaining acuity on crystal terminology in volcanic rocks". *Bulletin of Volcanology* 83, page 78. DOI: 10.1007/s00445-021-01513-y.